OXIDATIVE STEAM REFORMING OF LIGHT HYDROCARBONS IN A CATALYTIC MICROCHANNEL REACTOR

by

İrem Şen

B.S., Chemical Engineering, Bogaziçi University, 2010

Submitted to the Institute for Graduate Studies in
Science and Engineering in partial fulfillment of
the requirements for the degree of
Master of Science

Graduate Program in Chemical Engineering

Boğaziçi University

2013

ACKNOWLEDGEMENTS

I would like to express my gratitude to my supervisor Assoc. Prof. Ahmet Kerim Avcı, whose guidance and wise advices enlightened my way during my undergraduate and graduate years. Without his persistent help and encouragement, writing this thesis would not have been possible.

I would like to thank my thesis committee, Prof. Ramazan Yıldırım and Assoc. Prof. Hasan Bedir for devoting their valuable time to read and comment on my thesis.

My special thanks goes to Mustafa Karakaya for his endless patience to my never ending questions. I learned almost everything needed for my thesis from him, it was a great privilege for me to share the working environment with such a valuable person and a friend.

I want to thank everybody in KB 404 who makes my every day in there unforgettable. I was very lucky to be surrounded with great people like Eyüp Şimşek, M. İrfan Hösükoğlu, Gamze Gümüşlü, H. Onur Kavaklı, F. İdil Tezcan and Can Ekici.

I would like to express my inexpressible gratitude to Harun Ferit Özbakır for his irreplaceable friendship. Without him my graduate years would not have been so fun, easy and worth to remember. Tremendous thanks to my dearest colleague Cihan K. for being such a great support and constant source of strength for me especially for last months. Hope you always roll the hard six in your life! I would like to express my deepest appreciation to all my beloved friends who render each day in KB more enjoyable, especially Dilek Eren, Gizem Özbüyükkaya, Bahadır Kara, Oya Gürsoy Yılmaz, Z. Erge Akbaş, Begüm Alaybeyoğlu, Deniz Menekşedağ Erol, Aybike Nurocak, Melis Yıldırım , Serhat Erşahin, Fidan Sümbül and Arzu Uyar.

I wish to thank M. Selcen Başar for always being a good and supporting friend through last years; I learned so many things from her. Also I want to thank İpek

Paksoy for always welcoming me with her great smile. It was a real pleasure to work with you both and all the other people in CATREL team.

I also want to thank Elif Dereli, Ayça Cankorur Çetinkaya and Esra Börklü Yücel; assistantship duties would not be as fun and lively as it would be without you.

I would like to express my very special gratitude to Sevinç Genç and Seda Kizir for being my precious friends. Dreaming with you and making those become real with you is the most beautiful adventure I experience.

I want to thank my sisters Nihan Ünal and Merve Aygün for making me the luckiest person in the world by having you in my life. Life is as if we are always in Paris with you. I also owe so much to my friends with whom I shared many of the joys and great memories; especially Selin Sezen Çavuşoğlu, Burak Çavuşoğlu, M. Emre Esastürk, Beyza Bulutoğlu and Mehmet Z. Baykara. May the force be with you!

I cannot properly express my gratitude to my mother and father Ayfer and Recep Şen with just few sentences but I want to thank them for their endless support, love and patience. Special thanks to my brother Saitcan for always believing in me, encouraging me and making me smile even in the worst moments. I appreciate the moral support and friendship of my dearest aunt Şadiye Şen. My sincere thanks to Esin Doğu who made significant efforts on my education by her guidance and experience.

I also want to thank the departmental support staff Yakup Bal, Nurettin Bektaş, Bilgi Dedeoğlu, , Melike Gürbüz, Belgin Balkan, Canan Dedeoğlu and Başak Ünen for being always very kind to me and helping me whenever I asked for.

Finally, I would like to acknowledge TÜBITAK for granting me a scholarship. Financial support is provided by Boğaziçi University Research Fund through project BAP-6349.

ABSTRACT

OXIDATIVE STEAM REFORMING OF LIGHT HYDROCARBONS IN A CATALYTIC MICROCHANNEL REACTOR

Oxidative steam reforming (OSR) reaction of light hydrocarbons (methane and propane) is investigated under exhaust gas reforming (EGR) conditions in a catalytic heat-exchange integrated microchannel by computational and experimental techniques. OSR of propane is investigated by computer-based modeling and simulation studies to demonstrate the effects of different exhaust gas compositions from diesel and gasoline internal combustion engines (ICEs) by parametric variation of the amounts of propane and steam injected into the EGR feed and of the total feed flow rate. Steady-state simulations conducted using computational fluid dynamics (CFD) show that effective heat transfer and uniform temperature distribution can be obtained in the microchannel configuration even at low gas hourly space velocities (GHSVs). Higher H_2 and CO yields are possible by injecting more propane and steam into the feed. Increasing total feed flow rate, hence the GHSV improves axial heat distribution, but can lead to reduction in the H_2 and CO yields due to insufficient contact time. In the experimental part of the work, microfluidic EGR process is observed via OSR of methane over three different Pt- and Rh-based catalyst configurations. For each catalyst configuration, parametric study of methane OSR is conducted in order to observe the effects of feed compositions (molar steam-to-carbon (H_2O/C) and oxygen-to-carbon (O_2/C) ratios) and temperature on methane conversion and on product distribution. The results show that methane conversion is enhanced with the increase in temperature and in the amounts of O_2 and H_2O in the feed stream. The catalyst combination involving 2wt% Rh/Al_2O_3 coated catalyst only is found to exhibit the best performance in terms of increased methane conversion, and H_2 and CO compositions.

ÖZET

HAFİF HİDROKARBONLARIN OKSİJEN DESTEKLİ BUHAR REFORMLAMALARININ KATALİTİK MİKROKANAL REAKTÖR DÜZENİNDE İNCELENMESİ

Hafif hidrokarbonların (metan ve propan) oksijen destekli buhar reformlama reaksiyonları, egzoz gazı reformlama koşullarında ve mikrokanal reaktör düzeninde hesaplamalı ve deneysel yöntemlerle incelenmiştir. Propanın oksijen destekli buhar reformlama reaksiyonunun hesaplamalı çalışmaları, benzin ve dizel yakıtlı içten yanmalı motorlardan elde edilen farklı egzoz gazı bileşimlerinin, egzoz gazı reformlama reaktörüne beslenen propan ve buhar miktarlarının ve reaktöre beslenen toplam akış hızının sıcaklık ve ürün dağılımına etkilerini ortaya koymaktadır. Yatışkan halde yapılan hesaplamalı çalışmalar, mikrokanal reaktör düzeninde etkili ısı değişimininin ve homojen sıcaklık dağılımının düşük besleme hızlarında dahi sağlanabileceğini göstermiştir. Sisteme beslenen propan ve buhar miktarı artışının hidrojen ve karbon monoksit üretimini arttırdığı gözlenmiştir. Toplam besleme hızını arttırmak eksensel ısı dağılımını geliştirmiş fakat yetersiz kalma süresinden dolayı hidrojen ve karbon monoksit üretiminde düşüşe sebep olmuştur. Çalışmanın deneysel bölümünde reaksiyon sıcaklığının, molar buhar/karbon ve molar oksijen/karbon oranlarının Pt ve Rh bazlı kaplı katalizörler üzerinde gerçekleşen metanın oksijen destekli buhar reformlaması verimine olan etkileri mikroakışlı egzoz gazı reformlama koşullarında incelenmiştir. Sonuçlar metan dönüşümünün sıcaklık ve beslenen buhar ve oksijen miktarındaki artışla birlikte arttığını göstermektedir. Rh bazlı katalizörlerden oluşan kombinasyonun gerek metan dönüşümü gerekse de hidrojen ve karbon monoksit üretimi açısından daha iyi performans gösterdiği görülmüştür.

TABLE OF CONTENTS

LIST OF FIGURES

LIST OF TABLES

LIST OF SYMBOLS

A	Constant in heat capacity equation
A	Pre-exponential factor
A_s	Active surface area of catalytic washcoat (m^{-1})
B	Constant in heat capacity equation
c_{p_f}	Heat capacity of fluid($J\,kg^{-1}\,K^{-1}$)
c_{p_i}	Heat capacity of species i($J\,kg^{-1}\,K^{-1}$)
C	Constant in heat capacity equation
d	Depth of the microchannel (m)
d_{pore}	Average pore diameter of the catalyst (m)
D	Constant in heat capacity equation
D_h	Diameter of the housing (mm)
D_{il}	Binary diffusion coefficients ($m^2\,s^{-1}$)
$D_{i,m}$	Diffusivity of species i in the mixture $m^2\,s^{-1}$)
$D_{\text{eff},i,m}$	Effective diffusivity of species i in the mixture ($m^2\,s^{-1}$)
$D_{K,i}$	Knudsen diffusion coefficient for species i in ($m^2\,s^{-1}$)
E_a	Activation energy ($kJ\,mol^{-1}$)
F_{CH_4}	Molar flow rate of methane in reactor j ($mol\,s^{-1}$)
$\vec{\mathbf{F}}$	Momentum source/sink term ($kg\,m^{-2}\,s^{-2}$)
$\vec{g}$	Gravitational acceleration ($m\,s^{-2}$)
h_i	Sensible enthalpy of species i ($J\,kg^{-1}$)
H	Heigth of microchannel (mm)
ID	Inner diameter of the quartz tube (mm)
l	Length of the quartz tube (cm)
$\vec{J_i}$	Diffusive mass flux of species i ($kg\,m^{-2}\,s^{-1}$)
k_k^{ads}	Rate constant for the adsorption of k_sth species
k_k^{des}	Rate constant for the desorption of k_sth species
k_{eff}	Effective thermal conductivity of the fluid ($W\,m^{-1}\,K^{-1}$)
k_i	Thermal conductivity of species i ($W\,m^{-1}\,K^{-1}$)

k_f	Thermal conductivity of the fluid ($\mathrm{W\,m^{-1}\,K^{-1}}$)
k_s	Thermal conductivity of the washcoat ($\mathrm{W\,m^{-1}\,K^{-1}}$)
k_{SR}	Rate constant for the volumetric reaction SR
$K_{1,2}$	Equilibrium constants for SR
L	Length of the housing (mm)
M_i	Molecular weight of species i ($\mathrm{kg\,mol^{-1}}$)
N_g	Number of gas-phase species
$\vec{\mathbf{n}}$	Normal unit vector
p	Pressure (bar, kPa)
Q	Heat source due to chemical reaction ($\mathrm{W\,m^{-3}}$)
R	Universal gas constant ($\mathrm{J\,mol^{-1}\,K^{-1}}$)
$\mathcal{R}^{\mathrm{s}}_{k_s}$	Rate of k_sth surface reaction ($\mathrm{mol\,m^{-2}\,s^{-1}}$)
$\mathcal{R}^{\mathrm{v}}_{k_v}$	Rate of k_vth volumetric reaction ($\mathrm{mol\,m^{-3}\,s^{-1}}$)
s_0	Sticking coefficient
T	Temperature (°C)
T_{ref}	Reference Temperature (°C)
U^{in}	Normal inflow velocity (m)
v	Velocity (m/s)
v	Volumetric flow rate (Nml/min)
$\vec{\mathbf{v}}$	Velocity field ($\mathrm{m\,s^{-1}}$)
W	Width of microchannel (mm)
x_i	Mole fraction of species i
x, y, z	Cartesian coordinates (m)
Y_i	Mass fraction of species i
β	Temperature exponent
$\vert_{\Gamma_{\mathrm{gas}}}$, $\vert_{\Gamma_{\mathrm{solid}}}$	Gas/solid side of the gas-solid interface
ΔH^0_{298}	Standard enthalpy of reaction ($\mathrm{kJ\,mol^{-1}}$)
ΔH_i	Heat of formation of species i at temperature T ($\mathrm{kJ\,mol^{-1}}$)
$\Delta H_{i,ref}$	Heat of formation of species i at reference temperature ($\mathrm{kJ\,mol^{-1}}$)

ΔH_{rxn}	Enthalpy of reaction ($\mathrm{kJ\,mol^{-1}}$)
ΔT	Difference between maximum and exit channel temperatures (°C)
ϵ_{cat}	Porosity of catalyst j
ρ_f	Fluid density ($\mathrm{kg\,m^{-3}}$)
θ	Surface coverage
μ_i	Viscosity of species i ($\mathrm{kg\,m^{-1}\,s^{-1}}$)
μ	Viscosity of the gas mixture ($\mathrm{kg\,m^{-1}\,s^{-1}}$)
τ_{cat}	Tortuosity of catalytic washcoat
$\bar{\bar{\tau}}$	Stress tensor j due to flow ($\mathrm{kg\,m^{-2}\,s^{-2}}$)
σ_i	Stoichiometric coefficient of species i
χ_{CH_4}	Percent conversion of methane
ϖ_i	Collision diameter of species i
Ω_i	Collision integral of species i

LIST OF ACRONYMS/ABBREVIATIONS

2D	Two Dimensional
3D	Three Dimensional
ads	Adsorption
BET	Brunauer-Emmett-Teller
CFD	Computational Fluid Dynamics
des	Desorption
EDX	Energy Dispersive X-Ray Analysis
EGR	Exhaust-Gas Reforming
exit	Reactor exit
f	Fluid
FVM	Finite Volume Method
GC	Gas Chromatograph
GHSV	Gas Hourly Space Velocity
H_2O/C	Steam-to-Carbon Ratio
HPLC	High-Pressure Liquid Chromatography
i, k, l	Species indices
ICE	Internal Combustion Engine
in	Reactor inlet
k_s	Index for the surface reactions
k_v	Index for the volumetric reactions
max	maximum
MC	Microchannel
O_2/C	Oxygen-to-Carbon Ratio
out	Reactor outlet
OSR	Oxidative Steam Reforming
PDE	Partial Differential Equation
POX	Partial Oxidation
SEM	Scanning Electron Microscopy

SR	Steam Reforming
TCD	Thermal Conductivity Detector
total	Total amount
TOX	Total Oxidation
UDF	User-defined Functions
WGS	Water-Gas Shift

1. INTRODUCTION

The biggest portion of the world's energy demand is currently met by the fossil fuels, with the primary of them being crude oil. However it is well known that crude oil reserves are becoming depleted and their quality is decreasing. Because of these facts, alternative energy sources that can replace crude oil based products are being investigated in the last years. Since these products are most commonly used as fuels in the transportation sector, it is very important to replace them with renewable and sustainable alternatives.

Hydrogen seems to be one of the possible candidates for the replacement of crude oil based fuels in future; it is a very clean energy carrier, it reduces the emission of greenhouse gases and it is easily renewable since it can be produced from natural gas or other hydrocarbons as well as from the electrolysis of water. However, a large scale transition to hydrogen use as a fuel does not seem feasible before 2030. Therefore it is very important to improve emission and efficiency characteristics of the existing energy conversion technologies such as the internal combustion engines (ICE).

In the studies of transition between conventional ICEs and mobile hydrogen fuel cells, another technology, called exhaust gas reforming (EGR) has been proposed [1]. In this new system, a compact, catalytic reformer is integrated to the exhaust gas recirculation loop. External injection of a small amount of fuel to this reformer lets the autothermal reactions to occur over the catalyst which produces a hydrogen rich mixture. Oxygen and steam required for the reactions come from the exhaust gas. Feeding back the hydrogen rich mixture to the ICE improves its combustion efficiency and allows less amount of fossil fuel to be consumed for the same amount of work. Moreover, the undesired gas emissions are reduced [2].

Success of EGR depends on two important design aspects; catalyst type and the reactor configuration. The catalysts involving noble metals such as Pt and Rh are known to be the best options for driving oxidation and steam reforming of the injected

hydrocarbon, respectively. Energy needed for EGR is supplied by the sensible heat of the ICE exhaust stream and by the exothermal heat released by the combustion of the fuel injected into EGR. This heat should be utilized by endothermic fuel reforming, and, as a result, should be distributed fast and uniformly to the catalyst. Since rate of heat transfer is a strong function of reactor type, its choice is important for the efficiency of EGR. Current studies about EGR consider the use of either packed bed or monolithic reactors, and show that the latter is better in terms of heat distribution [3]. However the use of microchannel reactors in EGR has not been reported. These reactors are known for their improved mass and heat transfer properties due to their surface area-to-volume ratio which is much higher than those of conventional reactors. By reducing the heat transfer resistances, higher heat transfer coefficients can be obtained and autothermal reaction conditions of EGR can be satisfied.

This work investigates the use of a catalytic microchannel reactor at the conditions of EGR system. For this purpose, oxidative steam reforming (OSR) of propane and methane is investigated by using computational fluid dynamics (CFD) based modeling and experimental techniques, respectively. Modeling studies involve the simulation of OSR of propane, model hydrocarbon for gasoline [4], in microchannel reactor configuration at the EGR conditions. The catalytic microchannel reactor is designed to promote heat transfer between oxidation and reforming reactions and it is aimed to characterize temperature and product distributions at different modes and types of (gasoline and diesel fueled) ICE operation. The effects of addition of different amounts of propane and steam into the EGR feed, and of the total feed flow rate are also studied. In the experimental studies, a parametric study of methane OSR is conducted for understanding the effects of reaction temperature, catalyst type, feed compositions, namely molar steam-to-carbon (H_2O/C) and oxygen-to-carbon (O_2/C) ratios in the feed, on methane conversion and on product distribution.

The literature survey about microchannel reactors, EGR and OSR of methane and propane is given in Chapter 2. In Chapter 3 the techniques, procedures and equipment used in the experimental studies are explained in detail. Simulation studies about OSR of methane are described in Chapter 4 by giving a thorough explanation

of the mathematical model and related numerical solution techniques. Results and discussion of both experimental and computational work are given in Chapter 5. Finally in Chapter 6 major conclusions are reported and recommendations are given for the future studies.

2. LITERATURE SURVEY

2.1. Microchannel Reactors

Microchannel technology is a novel approach in chemical processing hardware offering many advantages such as increased efficiency and productivity. Devices called microchannel reactors offer advantages which make them highly attractive in the applications like highly exothermic reactions, fuel cells, screening for potential catalysts, high throughput materials synthesis and construction of micro plants [5]. Microstructured reactors provide significant size reduction so that reaction volumes decrease and better control on the systems can be achieved while mass and heat transfer rates and processing yields are enhanced [6].

Microchannel technology is characterized by the use of structured flow paths, i.e. channels with hydraulic diameters in the sub-millimeter range; characteristic diameters of the microchannels are between 10 to several hundred micrometers resulting in surface areas of 10000 - 50000 m^2/m^3 while in a conventional reactor this ratio is around 100 m^2/m^3 and rarely exceeds 1000 m^2/m^3 [7, 8]. The net result is volume reductions up to 90%, which leads to notable improvements in energy efficiency compared to the conventional process units [9]. To illustrate, the size of a conventional steam reformer which has block dimensions around 30 m $\times$ 30 m $\times$ 30 m can be reduced to 3.9 m $\times$ 5.8 m $\times$ 3.9 m via the use of microchannels [10]. Significant compaction also offers the possibility of transporting the processing units [11]. It is also predicted that the miniaturization in microstructured reactors decreases the amount of catalyst needed up to a factor of 1000 [7].

Compact nature of the microchannel units favors heat transfer, which is important for highly exothermic and endothermic reactions in terms of effective catalyst utilization, favoring isothermal operation and preventing hot spots formation [8, 12]. Using microchannels having improved heat transfer properties for the heat exchange, it is able to enhance the conversions of reactions when they proceed close to their ther-

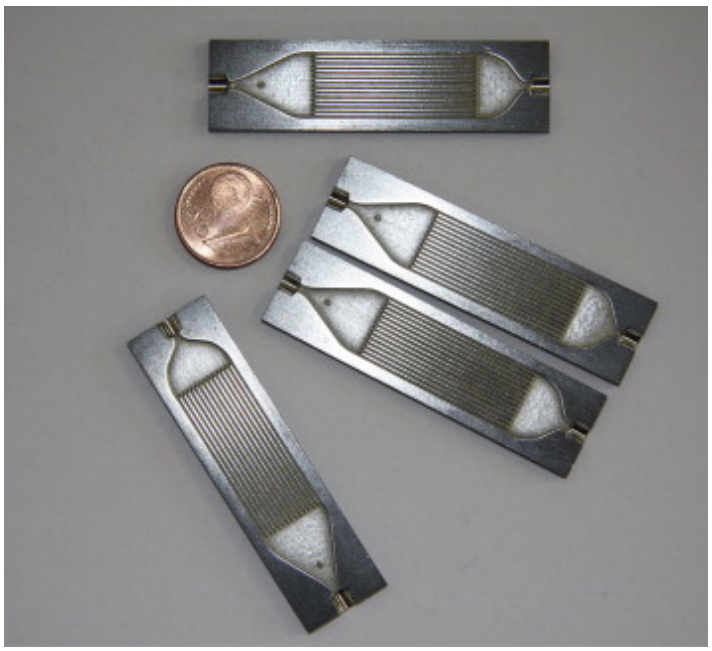

Figure 2.1. The microreactor.

modynamic equilibrium. Also this property gives the possibility to couple exothermic and endothermic reactions in a single reactor with heat exchanger design [12]. Mass transfer, just like heat transfer, is better in microreactors. Since laminar flow is fully developed in microchannels the Sherwood number, which is mass transfer coefficient multiplied by hydraulic diameter divided by the diffusion coefficient, reaches a constant value. This implies that as the hydraulic diameter gets smaller, the mass transfer coefficient gets larger, decreasing the mass transfer limitation [13].

In addition to the facts that hot-spot formation is avoided and the temperature control is well-established, flow amounts through the micro-flow units are considerably smaller when compared to the traditional reactors. These features give the opportunity of safer operations including the reactions characterized by near-explosive conditions, such as partial oxidations [14, 15]. Another beneficial feature of the micro sized units is the narrow residence time distribution. This increases the selectivity for production of specific material as it also enables easier scaling up by only increasing the number of units keeping the required geometry the same [16].

Microstructured devices are operated at laminar flow conditions in which heat

transfer coefficients are inversely proportional to channel diameter. For a typical microchannel reactor, heat transfer coefficients for liquids are about 10 kW/m^2.K which is an order of magnitude higher than those of conventional reactors [17]. Heat transfer coefficient around 25 kW/m^2.K with water as cooling medium is also reported [18]. Heat transfer coefficients have been demonstrated in other studies; in a steam methane reformer where the energy required for reforming is supplied by POX of methane in adjacent channels heat transfer rates for the exothermic reaction exceeded 18 W/cm^2 and total volumetric heat flux has reached 65 W/cm^3 while in a conventional reactor volumetric heat flux remained below 1 W/cm3 [10].

These properties make microchannel reactors promising for use in exhaust-gas-reforming (EGR) in which heat transfer is critical since in this process energy supplied by the sensible heat of the internal combustion engine (ICE) exhaust stream and by the exothermal heat of oxidation of the fuel injected into the reformer should be effectively transferred to the endothermic fuel reforming to favor the synthesis of a hydrogen-rich product [19].

2.2. Exhaust Gas Reforming

Exhaust gas reforming is a process which is used to improve the efficiency of the conventional internal combustion engines [1]. In this process presented in Figure 2.2, a reformer is integrated to the exhaust-gas recirculation loop. To this reformer a small amount of fuel is injected and it is allowed to be converted to hydrogen and carbon monoxide rich mixture by the reaction with steam and air over a selective reforming catalyst. This hydrogen-enriched mixture is then sent back to the engine [4]. The exhaust gas provides the co-reactants such as O_2, H_2O and CO_2 which are both required to convert the fuel. Also the necessary thermal energy to initiate exothermic reactions and sustain endothermic reactions on the catalyst (Table 2.1) is provided by the exhaust gas [19].

Sending hydrogen-enriched mixture to the engine has some beneficial effects. It is

Table 2.1. The reactions taking place in exhaust gas reforming [4].

Reaction	**Stoichiometry**	$\Delta \mathbf{H}^0_{298}$
Steam reforming	$C_xH_y + xH_2O = xCO + (y/2 + x)H_2$	<0
Partial oxidation	$C_xH_y + (x/2)O_2 = xCO + (y/2)H_2$	>0
Combustion	$C_xH_y + (x + y/4)O_2 = xCO_2 + (y/2)H_2O$	>0
Autothermal reforming	$C_xH_y + nO_2 + (2x - 2n)H_2O = xCO_2 + (2x - 2n + y/2)H_2$	0
Water gas shift	$CO + H_2O = CO_2 + H_2$	41 kJ/mol

reported that feeding the hydrogen-rich fuel back to the engine reduces the hydrocarbon and NO_x emissions in gasoline engines, breaks the "NO_x-particulate tradeoff" in diesel engines and promotes autoignition of various hydrocarbon fuels [4]. In engines addition of H_2 or H_2 rich reformate improves the overall engine efficiency and smoothes engine operation by reducing variations of cylinder pressure [1]. However, the main challenge for the application of EGR is the control of reformer inlet flows which the exhaust gas and fuel flows [20].

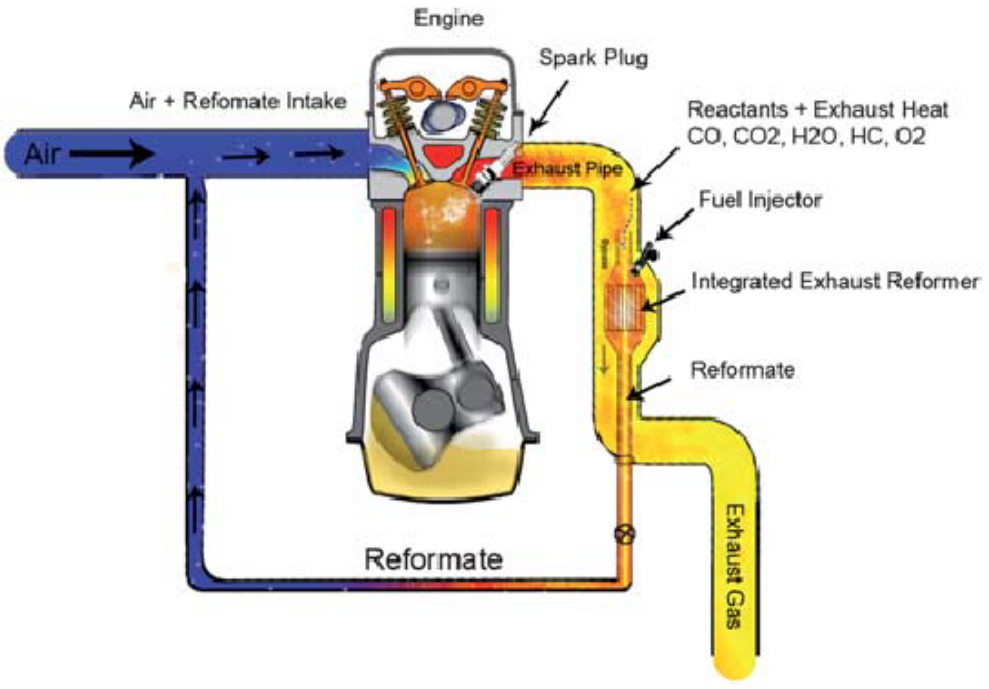

Figure 2.2. Schematic representation of exhaust gas reforming components [19].

In EGR, exhaust is used as a heat and co-reactants source during the conversion of small amount of fuel into reformate over a precious metal catalyst. The most commonly used EGR catalysts contain Pt and Rh as active metals and catalysts are generally bi-metallic. Support materials are ceria, zirconia and alumina [4]. It is known that Pt oxidizes SO_2 in the exhaust to SO_3, so by excluding it or using a more sulphur tolerant support material, less active but more sulphur tolerant catalyst may be designed [1]. In the absence of sulphur, it is seen that the lowest light-off temperatures are obtained for bimetallic Pt-Rh catalyst containing zirconia as a support are observed the catalysts containing Rh and base metal on zirconia free supports [4].

When it comes to the reactor design, the first thing to be satisfied is that the catalyst bed in the reformer must be functioning effectively under diverse conditions such as variable feed rates and inlet temperatures with minimal external control. Irrespective of the fuel type or reactor configuration, EGR process is characterized by the consecutive occurrence of total oxidation (TOX), steam reforming (SR) and water gas shift reactions at different stages of catalyst bed [3]. At lower reformer inlet temperatures, hydrogen concentrations up to 20% can be obtained by using both packed-bed or monolithic reactors. However at higher reformer inlet temperatures, higher hydrogen concentrations can only be applied in the monolithic reactors [3]. In the monolithic reactors increasing the catalyst bed length increases the catalyst amount where water-gas shift reaction is favored [20]. Water gas shift reaction is an exothermic reaction which represents a potential loss in efficiency by lowering the heating value of the reformate and generating waste heat rather than consuming it. So catalyzing water gas shift reaction is not desirable in EGR unless the amount of carbon monoxide is tried to be controlled carefully [19].

2.2.1. Microchannel Reactors in Oxidative Steam Reforming of Propane

Use of microstructured systems in reaction technology is a very new concept, and it offers many advantages in applications such as in SR, POX or oxidative steam reforming. Oxidative steam reforming combines the heat effects of combustion and SR reactions by taking both fuel, water and air as reactants [21]. In this section the

review of experimental and computational studies about microchannel reactor usage in oxidative steam reforming of propane will be given.

Oxidative steam reforming (OSR) of propane in Rh-impregnated metallic microchannel reactors was studied by Aartun *et al.* [22]. They manufactured the metallic microchannel monolith from Fecralloy having the composition of 72.6% Fe, 22% Cr and 4.8% Al. Their microchannel reactor had 676 channels and the dimensions of 5. 5mm × 5.6 mm × 20 mm (Figure 2.3).

Figure 2.3. Photograph of Rh-impregnated microchannel reactor [22].

For the manufacturing of Rh coated microchannels, the monolith was first oxidized in air at 1000°C and a thin layer of native aluminum oxide (alumina) is obtained. 1 mg of Rh is impregnated on this alumina layer by passing an aqueous solution of $RhCl_3$ through the channels and then the channels are dried at 120°C. The reduction of the monolith was done in situ at 800°C for 3 h in 10% H_2 in N_2. This monolith microchannel reactor were placed in a quartz tube and the experiments were carried out. The experimental apparatus in Figure 2.4.

The experiments were carried out using a continuous reactant flow at near-to-atmospheric pressure and furnace temperatures from 300 to 950°C where the total flow rate 1000 Nml/min. In OSR experiments, the reactant mixture consisting of propane, oxygen, steam and nitrogen having C/O and H_2/O ratios of 0.5 and 2.0 respectively, with N_2 to balance is sent to the reactor. At the specified total flow rate it was seen that gas phase ignition at the monolith entrance occurred at above 700°C. When the ignition happened at higher temperatures, the decrease in hydrogen production and increase in hydrocarbon by-products (methane and ethane) was observed. Also there was no catalyst deactivation reported.

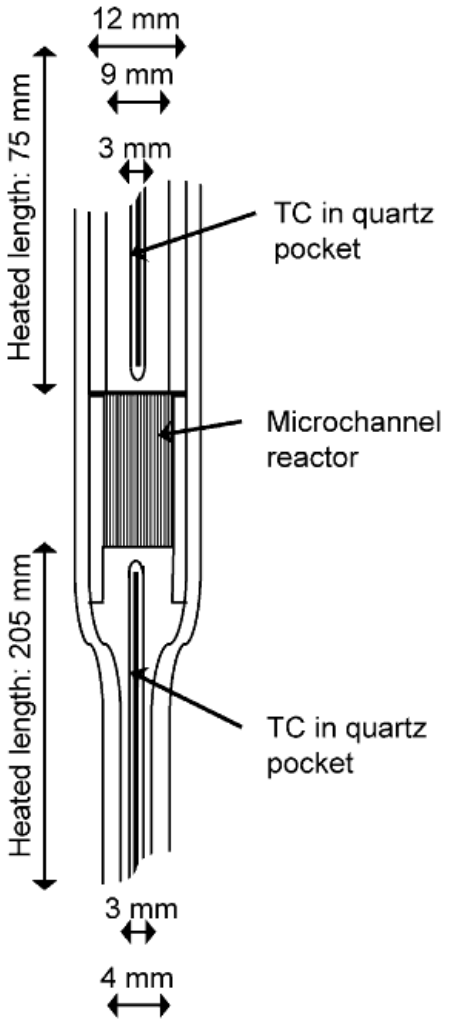

Figure 2.4. Schematic representation of quartz tube with microchannel monolith [22].

Aartun *et al.* [23] reported some other important results about temperature profiles and residence time effects during OSR in metallic microchannel reactors. According to their study, the temperature profiles obtained along the reactor axis proved that the usage of metallic microchannel reactor minimized the temperature gradients resulting from the exothermic nature of the OSR. They also investigated the effect of total flow rate and reported that at residence times less than 10 ms propane conversion increased as well as H_2 and CO selectivity. The production of undesired by-products such as methane and ethane is also reduced. This study also reported the stability of the Rh/Al_2O_3/Fecralloy microchannel reactor because no activation was observed even after 70 experiments performed in a wide range of temperature (300 to 1000°C).

Beside these experimental studies, catalytic combustion of propane on Pt was by Kaisare *et al.* [24] to understand the stability and performance of catalytic microreactors. They developed a pseudo-two-dimensional (2D) model to analyze the operation of Pt-catalyzed microreactors for propane combustion. They reported that the thermal conductivity of the reactor solid structure and inlet velocity have strong impacts on the heat and mass transfer rates along the microreactor. The microreactor became surface reaction limited at very low velocities and mass transfer limited at high velocities. The effect of reactor length was also studied and it was found that longer reactors are more stable when typical ceramics are used as a material of construction. At low velocities where the conversion is complete, the effect of reactor length is very small whereas the flow rate regime within which complete conversion is possible extended when longer reactors were used.

The performance of various catalysts on POX of propane was studied by Pennemann *et al.* [25]. This study is important because of its results about the performance of various catalysts based on Rh, Pd and Pt. Even though this study is about POX, the presence of water in the feed during the experiments makes it valuable for also OSR. The microstructured reactor used composed of two stainless steel plates each having 14 channels with dimensions of 500 μm width and 250 μm depth. γ-Al_2O_3 was used as a support material after it is calcined at 600°C. After the support is impregnated with metal solutions, it is again calcinated, but this time at 450°C. These catalysts

are washcoated into the channels and the microreactor was placed into a metal block equipped with a heating cartridge. The experiments were carried out within the temperature range of 700-850°C with O:C ratios in the range of $1.0 - 1.3$. Flow rates were adjusted to a total flow rate of 400 $\mathrm{Nml\,min^{-1}}$ with respect to the reactants, resulting in a GHSV of 274000 $\mathrm{h^{-1}}$ and an overall pressure drop of approximately 0.8 bar. Product gases were analyzed by an online gas chromatograph. The results showed strong dependency of propane conversion on catalyst type. Best results were reported while pure Rh or bimetallic Rh/Pt catalysts were used. It was reported that complete propane conversion was observed when Rh based catalysts were used. Also high selectivities towards H_2 and CO close the thermodynamic equilibrium is achieved for Rh-based catalysts. Bimetallic Rh/Pt catalyst is found to be as selective as pure Rh when the Rh concentration of the bimetallic catalysts was higher that 0.5 wt%.

A detailed kinetic analysis of TOX and SR of propane over 2% $Rh/\delta\text{-}Al_2O_3$ in annular microreactor was made by Pagani *et al.* [26]. $\alpha\text{-}Al_2O_3$ is used as a support material and incipient-to-wetness method is used to deposit $Rh(NO_3)_3$ onto it. Thin layers (15-30 μm) of catalytic powders were deposited on alumina tubular supports. A slurry was prepared by adding catalyst powders to an acidic solution; the alumina tubular support was coated on its terminal portion by dipping it into the slurry and extracting it at constant velocity. After the coated tube was dried at 280°C for 10 min a well adhered catalyst layer is obtained. The reactor is constructed by coaxially inserting the catalyst-coated ceramic tube into a quartz tube. The experiments were performed at atmospheric pressure within the temperature range of 300-800°C. The results show that H_2 and CO are formed through consecutive steps of TOX and SR of propane. It was found that C_3H_8 TOX was moderately inhibited by H_2O adsorption while SR was delayed in the presence of O_2. The rates of C_3H_8 TOX and the rates of C_3H_8 SR were proportional to the concentration of fuel; they showed a first-order dependence on fuel concentration.

2.2.2. Microchannel Reactors in Oxidative Steam Reforming of Methane

SR of methane is a very important reaction in hydrogen production. The process is characterized by high endothermicity (ΔH^0_{298} = 206.2 kJmol^{-1}) and sluggish reaction kinetics. These drawbacks can be overcome by coupling endothermic SR with exothermic methane TOX in the same reactor volume. This combined process, known as oxidative steam reforming of methane, has an autothermal nature such that the heat released by TOX is utilized by the endothermic SR.

Oxidative steam reforming of methane over Ni-based catalysts was studied by Tomishige *et al.* [27]. They compared Ni and Pt-based catalysts in oxidative steam reforming of methane. Al_2O_3 was used as a support and Ni and Pt-based catalysts are prepared by impregnating the support material with the aqueous solution of precursor. Pt and Ni loadings were arranged to be 1.5×10^{-4} mol g^{-1} cat^{-1}. The experiments are performed in a fixed bed quartz reactor under atmospheric pressure. The results showed that methane conversion over Pt/Al_2O_3 was considerably higher than over Ni/Al_2O_3. Also the temperature profiles along the catalyst bed showed that the distance between combustion and reforming zones are very short which is related to the reducibility of Pt that makes Pt to be maintained in metallic state in the combustion zone and under presence of oxygen. High energy efficiency was reported because the heat released by combustion was supplied to the SR reaction very effectively.

Li *et al.* [28], studied the temperature profiles of alumina-supported noble metal (Rh, Pt and Pd) catalysts in oxidative steam reforming of methane. Pt/Al_2O_3,Rh/Al_2O_3 and Pd/Al_2O_3 catalysts were prepared by impregnation method. Loading of the metals were arranged to be 3×10^{-5} mol g^{-1} cat^{-1}. The experiments are performed in a fixed bed quartz reactor under atmospheric pressure. The results showed the overlap of the combustion and SR zones most significantly on Rh-based catalyst but it was reported that this overlap led to a higher methane conversion and inhibition of the hot spot formation. As a result heat transfer efficiency was improved. These studies proved the advantages of noble metal usage because of their superior activity, selectivity and stability under harsh operating conditions.

Karakaya *et al.* [29] studied the SR of methane in a wall-coated catalytic microchannel reactor. Methane conversion and CO selectivity was studied by using Rh,Pt, Ru and Ni-based catalysts in the temperature range of 600-800°C and steam-to-carbon (H_2O/C) ratio range of 0.5-3.0. The comparison of packed bed and microchannel reactor was also given. The catalysts were prepared by incipient-to-wetness impregnation method. Catalytic microchannel was constructed by using FeCrAl sheets having the dimensions of 2 mm × 5 mm ×. These sheets were coated with the catalyst slurry and after drying process they are inserted into a stainless steel cylindrical housing. The reactor configuration is shown in Figure 2.5.

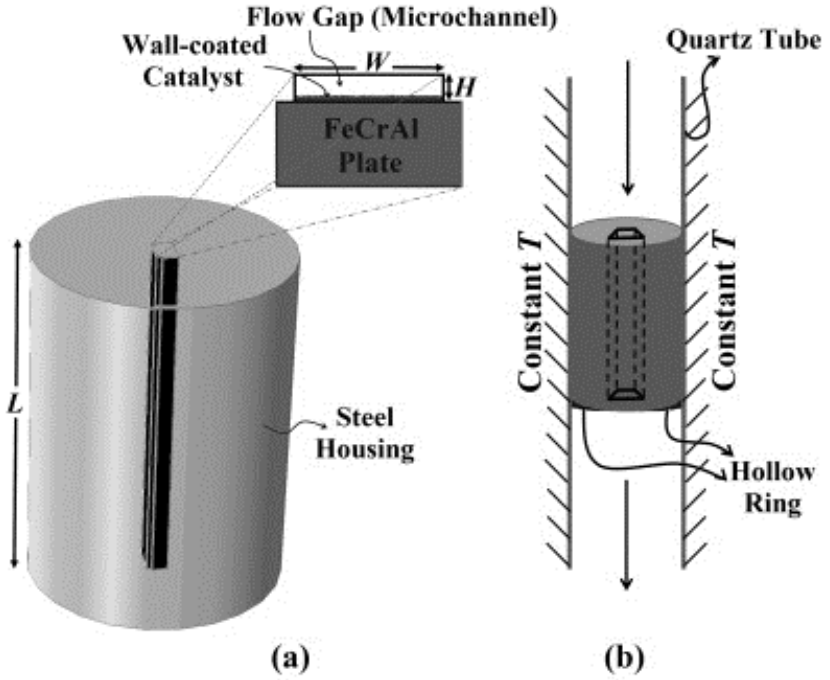

Figure 2.5. Orthographic drawing of the steel housing, the microchannel and the hollow ring inside the quartz tube [29].

Rh is reported to be the best one in terms of methane conversion and productivity, which is defined as the rate of methane consumption per weight of catalyst. The results show that with the increase in residence time, temperature and H_2O/C ratio, methane conversion increases for all catalysts. When CO selectivity was considered it was seen that Rh was again the best option. CO selectivity increases with the increase in temperature and decrease in H_2O/C ratio. Rh catalyst had excellent stability and

resistance to coke formation. These results were also compared with the conventional packed-bed reactors and it was reported that microchannel reactor had four- to six-fold increase in productivity and higher selectivity because of the improved heat and mass transfer rates.

Oxidative steam reforming of methane over an alumina supported bimetallic Pt-Rh catalyst was studied by Simsek *et al.* [30] in a coated and packed microchannel reactors. 0.2 wt%Pt - 2 wt%Rh catalyst was prepared by incipient-to-wetness impregnation method. Pt-Rh-alumina powder is mixed with deionized water to be blade coated on the FeCrAlY plates. After the coated plates are dried they are inserted into the H-shaped core of a cylindrical, stainless steel housing. After this housing is inserted into the quartz tube, the reactor became ready for experiments. Packed microchannel reactors are prepared by placing the particulate catalyst into an empty microchannel. These two types of reactors are represented in Figure 2.6. The experiments were conducted with the parameters of 500-750°C temperature, 0-3.0 H_2O/C ratio and 0.47-0.63 O_2/C ratio.

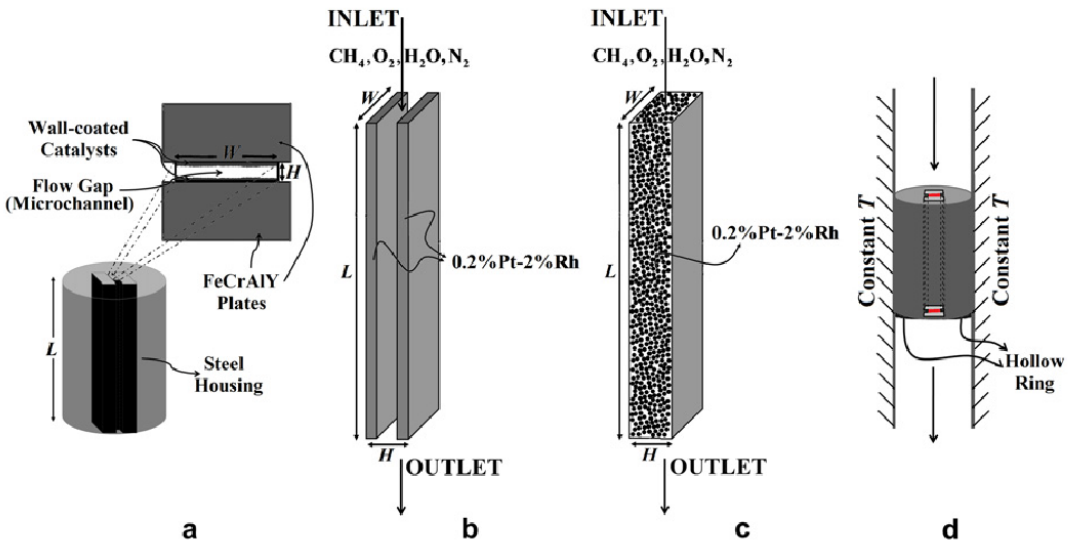

Figure 2.6. (a)H-shaped steel housing for two Pt-Rh coated plates and the catalytic microchannel, (b) coated microchannel reactor, (c) packed microchannel reactor, (d) location of the metal block inside the quartz tube [30].

The results showed that there was no significant difference between two types of reactor configuration in terms of methane conversion, however the coated one gave significantly higher CO selectivity than the packed one in the whole parameter range. Methane conversion increase with the increase in all parameters, but CO selectivity increased only with the increase in temperature and contact time. No catalyst deactivation was reported and a mechanical and chemical stability of the Pt-Rh catalyst was observed during the stable operation up to 72 h.

3. EXPERIMENTAL

3.1. Materials

3.1.1. Chemicals

All the chemicals used for catalyst preparation are presented in Table 3.1.

Table 3.1. Chemicals used for catalyst synthesis.

Chemicals	**Specification**	**Source**	**Molecular weight**
Rhodium(III) nitrate	$Rh(NO_3)_3$ $\sim$ 10wt%Rh in $>$ 5wt%nitric acid	Sigma-Aldrich	288.92
Tetraammineplatinum(II) nitrate	$[Pt(NH_3)_4](NO_3)_2$ 50.4wt%Pt	Sigma-Aldrich	387.22
Gamma alumina (3μm)	$\gamma - Al_2O_3$ $120 - 190\,m^2\,g^{-1}$	Merck	——
FeCrAlY	FeCrAlY sheets	Goodfellow Cambridge	——

3.1.2. Gases and Liquids

All of the gases used in this work were supplied by Linde Gas Turkey, Istanbul. Table 3.1 lists the specification application of each gas. Besides the listed items in Table 3.2 deionized water with conductivity less than 0.1 μS cm^{-1} is used in all experiments.

3.2. Experimental System

The experimental system used in this work mainly consists of four groups:

- Catalyst Preparation System: the system used to prepare the support and synthesize the catalysts by the incipient-to-wetness impregnation method
- Catalytic Reaction System: the system used to observe catalytic reactions and to determine the catalytic activity, consisting of mass flow controllers for inlet gases, HPLC pump for water feed, electric heat tracing, reaction chamber and

Table 3.2. Specifications and applications of the gases used.

Gas	**Specification**	**Application**
Argon	99.999% (Linde)	GC carrier gas
Helium	99.999% (Linde)	GC carrier gas
Carbon monoxide	99.999% (Linde)	GC calibration
Hydrogen	99.99% (Linde)	GC calibration, reduction
Carbon dioxide	99.999% (Linde)	GC calibration, reduction
Oxygen	99.998% (Linde)	GC calibration, reactant
Methane	99.9% (Linde)	GC calibration, reactant
Nitrogen	99.998% (Linde)	Inert

feed/product sampling sections

- Product Analysis System: the system used to determine the composition of the feed and product streams quantitatively, consisting of two gas chromatographs

3.2.1. Catalyst Preparation Systems

The system used for catalyst preparation by incipient-to-wetness impregnation method (Figure 3.1) consists of a Retsch UR1 ultrasonic mixer which provides uniform mixing and contacting of the solution with the support, a vacuum pump, a Buchner flask, silicone tubing and a Masterflex computerized-drive peristaltic pump which is used for addition of the solution to be impregnated.

3.2.2. Catalytic Reaction System

The catalytic reaction system was designed and constructed at the Department of Chemical Engineering, Catalyst Technology and Reaction Engineering Laboratory (CATREL). This system mainly consists of three characteristic sections:

- Feed section
- Reaction section
- Product analysis section

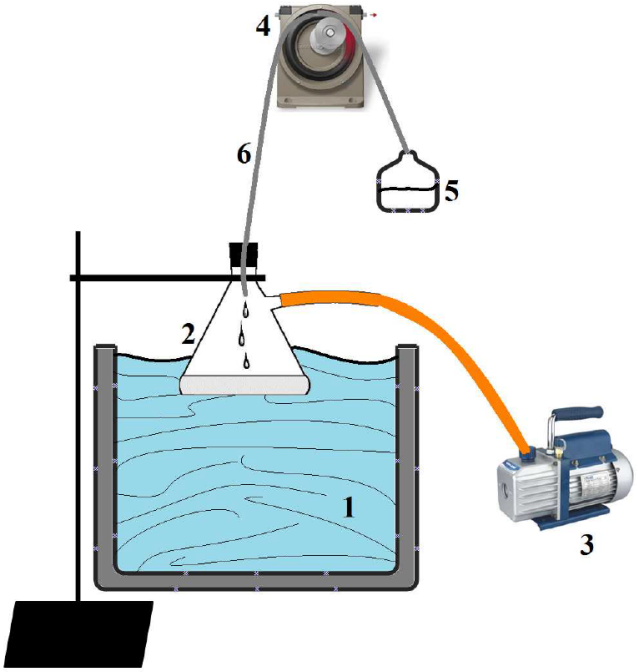

Figure 3.1. Schematic representation of impregnation system. 1. Ultrasonic mixer, 2. Buchner flask, 3. Vacuum pump, 4. Peristaltic pump, 5. Aqueous catalyst solution, 6. Silicon tubing (1.6 mm ID) [31].

Feed preparation section consists of mass flow controllers, 1/4", 1/8" and 1/16" stainless steel tubes and fittings for feeding water and gaseous species, i.e. nitrogen, methane, carbon dioxide and oxygen precisely. Gas regulators are used to regulate the gas flow from pressurized storage cylinders to the system. Bronkhorst F-201CV series digital mass flow controllers are used to measure and control the flow rates of the gases. Calibrations of these mass flow controllers were also done and calibration curves are given in Appendix A. Each gas is attached to the system by using different lines so that flow of gases can be measured independently and desired feed compositions can be adjusted easily. Deionized water is fed to the system by using Shimadzu LC-20AD HPLC pump with constant and pulse-free flow. Liquid water is vaporized before mixing with the gases and sending to the reaction chamber in the 1/16" tube. This tube is kept at 120±3°C using a 1 m heating tape, a 16-gauge wire K-type sheathed thermocouple and a four-channel temperature controller. Then gas mixture and steam are mixed in the mixing zone before entering the reaction chamber since it's very important to feed homogeneous mixture into the reactor. The temperature of the mixing zone is also

measured and controlled by a 16-gauge wire K-type sheathed thermocouple and the temperature controller. The first data is taken in 30^{th} minute after the reaction started, then data is taken in every 45 minutes. The reported results belong to the arithmetic average of the data after the system reaches to the steady state which approximately corresponds to the second hour of the experiment.

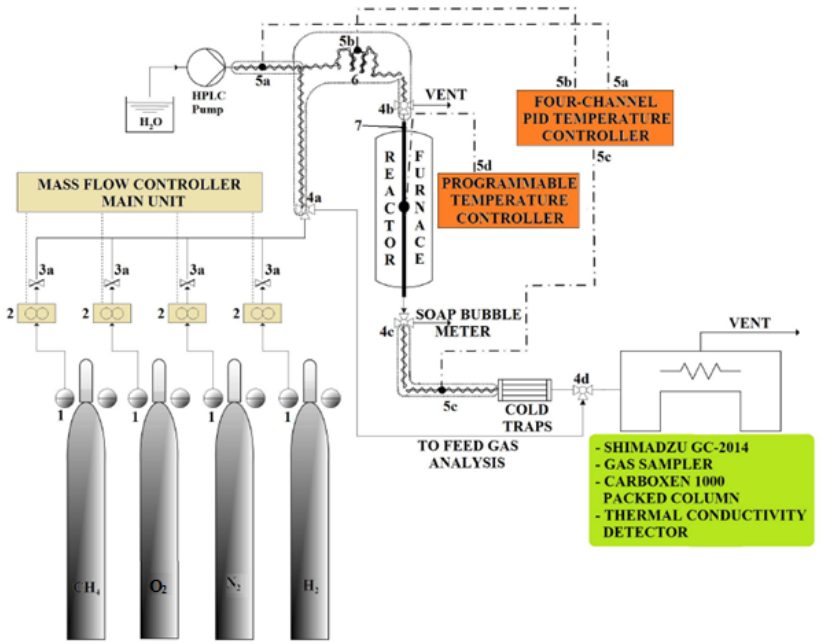

Figure 3.2. Schematic representation of the reaction system. 1. Gas regulators, 2. Mass flow controllers, 3. On-off valves, 4. Three-way valves, 5. Thermocouple locations, 6. Mixing zone, 7. Quartz tube [31].

In order to have better control on flow, three-way valves are installed to the piping system which makes possible to divert the flow upon need. Valves 4a and 4d are used to send gases directly to the gas chromatograph when feed gas analysis is to be performed, i.e. the composition of the reactant stream prior to reaction is to be determined. Valve 4b is used to switch flow between the reactor line and the vent. It is very important to vent off the reactant mixture approximately for 30 min before the reaction to provide steady and well-mixed feed flow. In the product stream leaving the reactor, water is kept in vapor phase by adjusting the temperature of the line between Valve 4c and the cold traps to 120°C. Control of total gas flow rate at the reactor

exit is done before system testing by using a soap bubble meter, which is also used to monitor the gas flow during reaction tests. In order to remove water vapor in the product mixture before entering the GC unit, two salt-ice cold traps placed in the Dewar flasks are used. Detailed description of the product analysis using GC is given in the following section.

3.2.3. Product Analysis System

The product stream consists of -on a dry basis- unconverted methane, hydrogen, carbon monoxide and dioxide, inert nitrogen, and trace amount of other light hydrocarbons such as ethane and propane. All these species is quantified by using a Shimadzu GC-2014 gas chromatograph, equipped with Carboxen 1000 packed column and a thermal conductivity detector (TCD). Calibration of both chromatograph units is done before reaction tests by injecting the known volumes of each species through the injection ports to the column under the conditions given in Table 3.3. In the chromatograph each species forms a peak, area of these peaks are calculated by integration and then plotted against the known volumes to construct the calibration curves which are presented in Appendix B.

Table 3.3. GC conditions for product analysis.

GC Parameter	**Shimadzu GC-2014**
Detector type	TCD
Column temperature	40° C (0 → 13.5 min) 40 →150° C (13.5 → 15.5 min) 150° C (15.5 → 23.5 min)
Injector temperature	110° C
Detector temperature	175° C
Detector current	50 μA
Carrier gas	Ar
Carrier gas flow rate	25 ml.min^{-1}
Column packing material	Carboxen 1000
Column tubing material	Stainless steel
Column length & ID	6 m & 3 mm
Sampling loop	1 ml kept at 25° C

3.3. Catalyst Preparation and Pretreatment

3.3.1. Support Preparation

Catalytic oxidation and SR of hydrocarbons, especially those of methane, occur at high temperatures. Therefore, the catalyst support should not only have high surface areas, but also have high thermal stabilities. Due to its high surface area γ-Al_2O_3 is the most preferred support material. However, it has been reported to have lower stability at temperatures greater than 600°C and it has a tendency to experience carbon formation in the presence of steam due to its high acidity [32]. The most thermally stable phase of alumina is obtained when the γ phase is transformed into the α phase at temperatures greater than 1127°C [33]. However, its low surface area, which is less than 5 m^2g^{-1}, is likely to result in poor catalytic activities due to the low dispersion of active metals. Using a support such as δ-alumina–an intermediate phase between γ and α–, having relatively high thermal stability and a decent surface area is optimum in terms of catalytic performance [32]. Three different support preparation procedures were investigated by Avci and coworkers as given in Table 3.4 [34]. They basically involved the calcination of γ-Al_2O_3 (BET surface area: 279 m^2g^{-1}) at various temperatures. Comparison of the resulting materials was based on their BET surface areas.

Table 3.4. Al_2O_3 support preparation procedures [34].

Procedure	**BET surface area (m^2g^{-1})**
Calcination at 1000°C for 4h	46.8
Drying of Al_2O_3 at 150°C for 2h followed by calcination at 900°C for 4h	81.6
Drying of Al_2O_3 at 105°C overnight followed by calcination at 875°C for 4h	73.2

In Table 3.4 it is seen that the second procedure resulted in the highest BET surface area. From comparison of these procedures (especially the last two ones), it is appeared that the duration of drying is important because a longer period of drying

at a lower temperature resulted in a lower surface area, even though the calcination temperature was less than that for the second procedure. The experimental tests in this work are done for oxidative steam reforming (OSR) of methane for the parametric study of microchannel (MC) reactor configurations. A set of Xwt% M/δ-Al_2O_3 catalysts (M = Rh and Pt) with varying metal loadings (X = 2 for Rh and Pt, 0.2 for Pt) are prepared by the incipient-to-wetness impregnation method for the experiments. Alumina powder of 3-μm size (Table 3.1) is used for synthesizing the MC catalysts. Thermally stable δ phase of both supports are obtained by drying at 150°C for 2 h and calcination at 900°C for 4 h in accordance with the procedural guidelines given in Table 3.4.

3.3.2. Preparation of Active Catalysts

3.3.2.1. Incipient-to-wetness Impregnation of Active Metals. The incipient-to-wetness impregnation method is a very common technique in microchannel catalyst syntheses. At the first stage, the calculated amount of metal precursors given in Table 3.1 are dissolved in certain amount of deionized water (ca. 1 $ml_{solution}$ $g^{-1}_{support}$). Then the support (3 μm sized γ-Al_2O_3) is mixed ultrasonically for 25 min under vacuum in Buchner erlen. By using a peristaltic pump the prepared aqueous solution of the metal precursor is impregnated over the support (Figure 3.1). The resulting slurry is mixed ultrasonically for 1.5 h again under vacuum, and is dried overnight at 120°C. Finally, the catalyst is calcined at 500°C at a ramping rate of 5°C min^{-1} for 3 h.

3.3.2.2. Catalytic Microchannel Synthesis. The preparation of catalytic microchannels is a challenging process consisting of several mechanical and chemical treatment methods. At first stage, FeCrAlY sheets (Table 3.1) are cut into 2 mm × 5 mm × 20 mm plates by using wire electro discharge machining. Also a cylindrical housing (diameter D_h = 18.6 mm, and length L = 30 mm) is prepared by using the same technique from 310-grade stainless steel. These prepared plates are then calcined in air at 900°C at a ramping rate of 20°C min^{-1} for 2 h to enhance the adhesion of the coated plates by forming a native alumina layer on the plates. In order to prepare catalyst slurries, the previously calcined 3-μm δ-Al_2O_3 supported catalyst powders are mixed

with deionized water at a water-to-powder weight ratio of 5 - 8 : 1. The resulting slurries are blade-coated onto the 5 mm × 20 mm plates till the weight per surface area reaches ca. 0.02 $g_{cat}cm^{-2}$. These coated plates are dried at 120°C overnight, and then they are calcined at 500°C for 3 h. After the catalyst coated plates are ready, they are inserted into the cylindrical housing. The interior of the housing is engineered by wire electro discharge machining to have a combined opening for the plates and the microchannel. Two plates coated with Pt/δ-Al_2O_3 and Rh/δ-Al_2O_3 are inserted with 0.5 mm fitting to the grooves at each side so that one microchannel having the dimensions of height H = 0.75 mm, width W = 4 mm and depth d = 20 mm is obtained. Before the plates attached to the reaction chamber, catalyst coated plates are inserted into the housing and then they are removed in order to let the grooves to strip off some coating on the side of the plates, after this procedure the net weight of the catalysts are measured. There is one more step to fix the position of the plates in the housing since there is 10 mm gap between the bottom of the catalytic plates and the bottom of the housing. This gap is stuffed with ceramic wool so that a possible displacement of the plates is prevented. Figure 3.3a shows the orthographic drawing of the "H-type" cylindrical housing and the synthesized catalytic microchannel used in the oxidative steam reforming of methane. In Figure 3.3b the catalyst arrangement is depicted, as can be seen from the figure the reactive mixture consisting of methane, steam, oxygen and nitrogen flows top down through the microchannel reactor.

3.3.3. Pretreatment

Catalysts should be activated after calcination process. The reason behind this action is to reduce the active metals from their oxidized states to the metallic state. This operation is done in situ under 40 Nml min^{-1} hydrogen flow at 800°C for 2 h before the reaction tests.

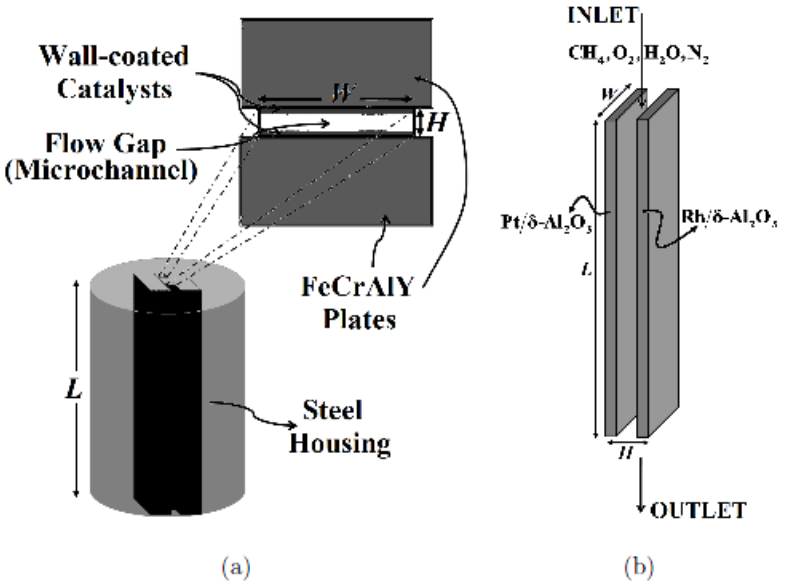

Figure 3.3. (a) Orthographic drawing of the steel housing and the microchannel used in experiments, (b) details of the catalytic microchannel configuration [31].

3.4. Reaction Tests

3.4.1. Blank Tests

The reason to conduct blank tests before reaction tests is to ensure that the materials of construction (stainless steel and FeCrAlY), glass and ceramic wools, and δ-Al_2O_3 (used as diluent) are inert toward the reactants. During blank tests reactor effluents are analyzed in GC using only uncoated plates and the results show that there is not any oxidation or SR activity.

3.4.2. Autothermal Reforming of Methane in Microchannel Reactor

Microchannel experiments are done by using quartz tube, H-type housing and two coated plates (with 0.2wt%Pt/δ-Al_2O_3 and 2wt%Rh/δ-Al_2O_3). The housing which contains the catalyst coated plates is placed into the center of the quartz tube having inner diameter ID = 20 mm and length l = 80 cm. The housing is supported underneath by a hollow ring that is wide enough in order to ensure sufficient circumferential

overlap as can be seen in Figure 3.4. This design keeps the housing stationary in the desired position and prevents bypass through the annulus between the housing and the tube. During the experiments, bypass is also diminished due to the thermal expansion of the steel housing at high (> 500°C) temperatures. Temperature control of the catalytic zone is done by Shimaden FP-23 programmable temperature controller and a K-type sheathed thermocouple. This measurement is done with the precision of ±0.1°C. Thermocouple has immediate contact with the central point of the quartz tube in which the catalytic microchannel is located. The quartz tube is placed in the furnace such that the middle part of it, i.e. the catalytic zone stays within the 10 cm constant-temperature zone.

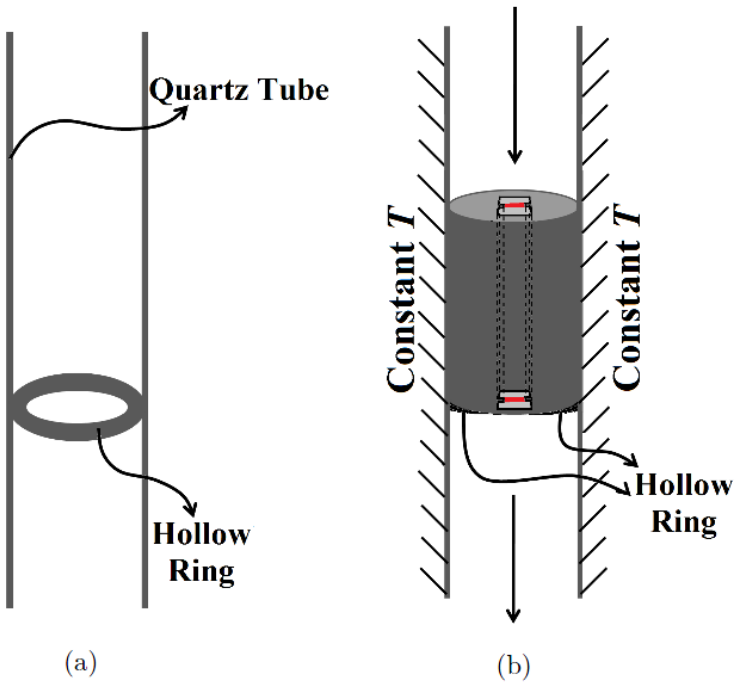

Figure 3.4. (a) The hollow ring inside the quartz tube, the microchannel reactor arrangement inside the quartz tube (b) for steam and (c) autothermal reforming of methane [31].

In MC experiments the effects of (i) reaction temperature between 600 and 700°C, (ii) steam-to-carbon ratio (H_2O/C) between 1 and 1.5, (iii) oxygen-to-carbon ratio (O_2/C) are investigated. Total flow rate of the reactant gases is kept constant at 90 ml/min during each experiment. H_2O/C ratio is defined as the number of moles of steam divided by that of methane at the inlet. O_2/C ratio is defined as the number

Table 3.5. Operating conditions studied in methane OSR experiments.

Operating parameters	**Parameter values**
Temperature (°C)	600, 650, 700
H_2O/C (mol/mol)	1, 1.25, **1.5**
O_2/C (mol/mol)	0.5, 0.75, **1**

Table 3.6. Feed conditions for OSR of methane experiments.

Catalyst Type	**CH_4 (ml/min)**	**CO_2 (ml/min)**	**Total Flow Rate (ml/min)**
0.2%Pt-2%Rh	15	9.3	90
2%Pt-2%Rh	15	9.3	90
2%Rh-2%Rh	15	9.3	90

of moles of oxygen divided by that of methane at the inlet. Mole fraction of methane is kept constant at 0.167 in all runs. The H_2O/C and O_2/C ratios are adjusted by varying the H_2O and O_2 flow rates, respectively. N_2 flow rate such that the total flow rate of the reactants and partial pressure of methane remain unchanged. The experimental program is summarized in Table 3.5. Parametric studies to observe the effect of H_2O/C are done by taking O_2/C ratio of 1 as default and parametric studies to observe the effect of O_2/C are done by taking H_2O/C of 1.5 as default, these default values are shown in bold in Table 3.5 . The methane conversion (χ_{CH_4}) is calculated by simply calculating the percent difference of CH_4 in inlet and outlet streams as stated by Eq. 3.1.

$$\chi_{CH_4} = 100 \times \frac{F^{in}_{CH_4} - F^{out}_{CH_4}}{F^{in}_{CH_4}} \tag{3.1}$$

4. MODELING AND SIMULATION

This chapter explains the construction and development of the mathematical model of the heat exchange integrated microchannel reactor. Using computational fluid dynamics (CFD) model is used to simulate reactive flow and transport phenomena occurring inside the system. In this work oxidative steam reforming reactions of propane inside a heat exchange integrated microchannel reactor with Rh and Pt- based catalysts is investigated. Reaction kinetics, physical properties, microchannel geometry and flow configuration is obtained from literature and handled separately.

4.1. Exhaust Gas Reforming Process

In exhaust gas reforming some amount of fuel is injected to the exhaust gas coming from an internal combustion engine (ICE) in order to produce H_2 rich mixture. Energy supplied by the sensible heat of the ICE exhaust stream and by the exothermal heat of oxidation of the fuel injected into the reformer should be effectively transferred to the endothermic fuel reforming to favor the synthesis of a hydrogen-rich product [19]. This process is investigated on the basis of operating conditions such that air-to-fuel molar inlet ratio (O_2/C) and steam-to-carbon molar inlet ratio (H_2O/C) and total flow rate.

The gaseous fuel used in this work is propane which is suggested to be a model hydrocarbon for gasoline [4]. Exhaust gas properties describing low, medium and high-load modes of gasoline and diesel fueled ICEs [3, 4, 20] are summarized in Table 4.1 and Table 4.2, respectively. The inlet feed given in these tables also contains balance nitrogen and the given percentages of C_3H_8 belongs to the amount of fuel added to the reformer. The reactions taking place are given in Equations 4.1 and 4.2. Kinetics of propane oxidation over Pt/δ-Al_2O_3 and SR over Rh/δ-Al_2O_3 are obtained from the literature [24, 35]. The effects of homogenous reactions are neglected. In all cases, the total feed flow rate, corresponding to a GHSV (total feed flow rate/volume of the coated catalyst layers) of 22000 h^{-1}, is kept constant at 43.75 ml/min. Reactions

are simulated at atmospheric pressure, and gas mixtures are assumed to follow ideal, incompressible Newtonian fluid behavior.

Constant values of species mass diffusivities and correlations used to estimate densities, thermal conductivity and viscosity of the species are obtained from the literature [36–40]. Effective diffusivity of the washcoat layer is taken as the one half of the obtained gas phase effective diffusivity [41]. Effective thermal conductivities of the fluids in the TOX and SR washcoats are taken as 4.2 and 4.5 times the respective bulk fluid conductivities [41]. Porosity of the washcoat layers is taken as 0.4 [41].

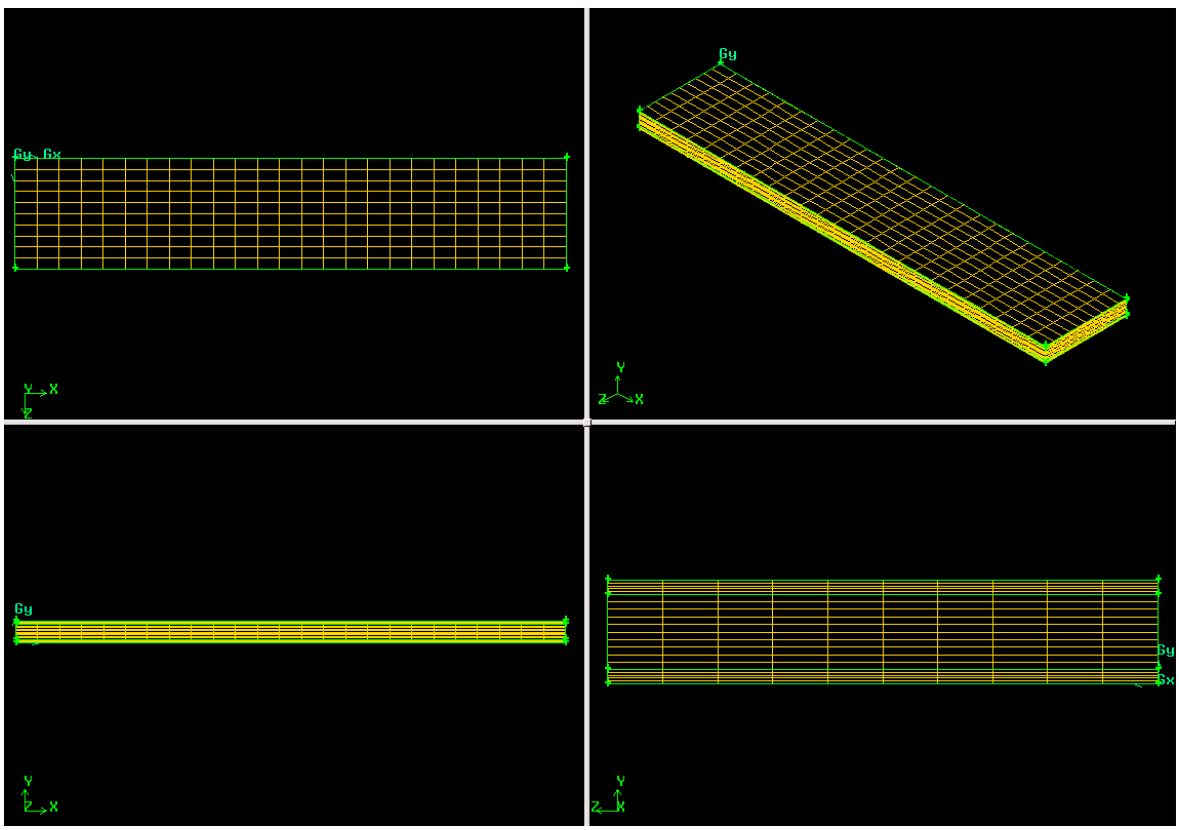

Figure 4.1. The grids used in the simulations of the 3D microchannel.

3D geometry of the channel is given in Figure 4.3. 3D continuity, momentum, species mass and energy conservation equations are solved using the finite volume method (FVM) on the computational fluid dynamics package FLUENT^{TM} 14.0 [42]. The 3D Cartesian grid consisting of 8.75 $\times$ 10^5 rectangular cells is constructed using the preprocessing software GAMBIT 2.4.6. (Figure 4.1). The grid is refined in the

catalytic washcoat domains since steep concentration and temperature gradients are expected to occur due to reaction kinetic characteristics.

The pressure-velocity coupling is done by the pressure-based solver that uses the SIMPLE algorithm and the gradients are calculated by the least squares cell-based scheme. The PRESTO! discretization scheme is applied for the pressure while the second-order upwind scheme is applied for the momentum and species conservation equations [42]. Combustion kinetics and concentration-dependent viscosity and diffusivities are implemented in the code and evaluated in each associated cell by means of user-defined functions (UDF), which access the species mass fractions in that cell during each iteration.

Table 4.1. Product compositions of the exhaust stream from gasoline fueled ICE [4].

Case	$\mathbf{O_2/C}$	$\mathbf{H_2O/C}$	**T** (°**C**)	$\mathbf{O_2}$ (%)	**CO** (%)	$\mathbf{CO_2}$ (%)	$\mathbf{H_2O}$ (%)	$\mathbf{C_3H_8}$ (%)	$\mathbf{v^*_{total}}$ (Nml/min)
1	0.07	2.08	400	0.4	0.3	12.9	12.5	2	43.75
2	0.45	0.55	350	6.8	0.14	9.3	8.3	5	43.75
3	0.46	0.23	350	10.7	0.14	5.9	5.6	8	43.75
2a	0.45	0.55	350	6.8	0.14	9.3	8.3	5	21.88
2b	0.45	0.55	350	6.8	0.14	9.3	8.3	5	87.50
2c	0.45	0.55	350	6.8	0.14	9.3	8.3	5	131.25
2d	0.45	0.28	350	6.8	0.14	9.3	4.2	5	43.75
2e	0.45	1.11	350	6.8	0.14	9.3	16.6	5	43.75
2f	0.45	1.66	350	6.8	0.14	9.3	24.9	5	43.75

*v_{total} is the total volumetric flow rate fed to the catalytic microchannel reactor.

Table 4.2. Product compositions of the exhaust stream from diesel fueled ICE [3, 20].

Case	$\mathbf{O_2/C}$	$\mathbf{H_2O/C}$	**T** (°**C**)	$\mathbf{O_2}$ (%)	**CO** (%)	$\mathbf{CO_2}$ (%)	$\mathbf{H_2O}$ (%)	$\mathbf{C_3H_8}$ (%)	$\mathbf{v^*_{total}}$ (Nml/min)
4	0.61	0.42	370	9.1	0.01	6.4	6.2	5	43.75
5	0.79	0.32	290	11.9	0.01	4.8	4.7	5	43.75
6	0.95	0.27	240	14.3	0.01	4.3	4.1	5	43.75
7	1.05	0.22	200	15.8	0.01	3.3	3.3	5	43.75

*v_{total} is the total volumetric flow rate fed to the catalytic microchannel reactor.

4.1.1. Production of Hydrogen-rich Exhaust-Gas Effluent

4.1.1.1. Oxidative Steam Reforming of Propane. Oxidative steam reforming of propane, surrogate for gasoline and diesel, basically consists of two reactions: SR and TOX which are endothermic and exothermic, respectively. In the modeled exhaust gas reforming system, the heat required for the SR of propane is supplied by the TOX reaction of propane. The stoichiometric reactions occurring and the enthalpies of reactions are presented by Equations 4.1 and 4.2. As given in Table 2.1, there is also water gas shift reaction involved in exhaust gas reforming process, but in the simulations this reaction is ignored due to lack of kinetic data. Since this is a parametric study to investigate the effect of O_2/C and H_2O/C ratios, that kind of assumption can be done.

$$C_3H_8 + 5O_2 \rightarrow 3CO_2 + 4H_2O \qquad \Delta H^0_{298} = -2044 \text{ kJmol}^{-1} \tag{4.1}$$

$$C_3H_8 + 3H_2O \rightleftharpoons 3CO + 7H_2 \qquad \Delta H^0_{298} = 498 \text{ kJmol}^{-1} \tag{4.2}$$

4.2. Heat Exchange Integrated Microchannel Reactors

4.2.1. Microchannel Reactor Model

The microchannel reactor involves parallel, rectangular-shaped channels with dimensions of height H = 7.5×10^{-4} m, width W = 4×10^{-3} m and length L = 2×10^{-2} m. 1×10^{-4} m thick layers of porous Pt/δ-Al_2O_3 and Rh/δ-Al_2O_3 catalysts, driving propane TOX (Eq. 4.1) and propane SR (Eq. 4.2) respectively, are considered to be washcoated into the inner channel walls facing opposite to each other. Due to the particular positioning of the channels and catalyst layers, heat transfer is assumed to occur only within the channels (i.e. between the Pt and Rh layers); heat exchange between the channels, i.e. in the y- and z- directions are neglected and a single, adia-

batic channel is taken as the characteristic unit of the multichannel device as shown in Figure 4.2. Also the microchannel is assumed to be perfectly isolated on the outermost so that heat loss to the surroundings can be neglected.

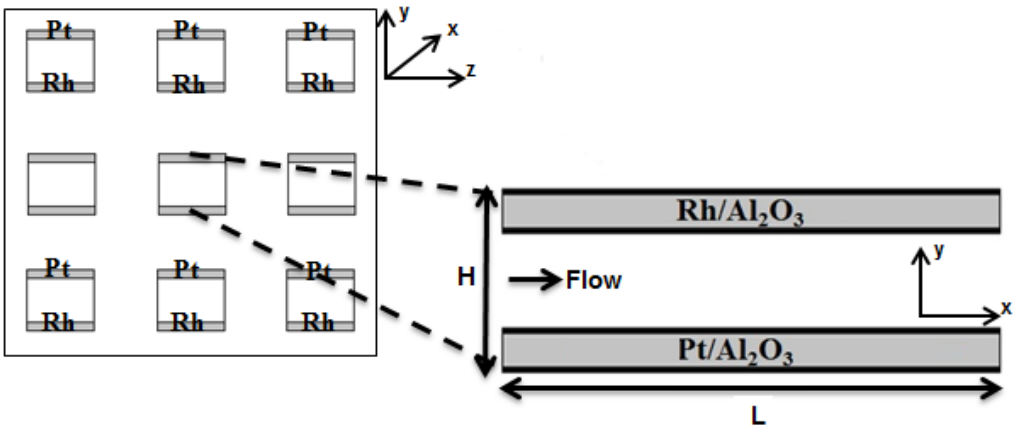

Figure 4.2. Schematic representation of the heat exchange integrated microchannel system.

The flow and transport equations are applied in 3D Cartesian coordinates. 3D representation of the microchannel is represented in Figure 4.3. Reactant stream flows inside the channel and heat transfer is observed inside the channel. Washcoat domain contains the porous catalyst and it is assumed that reaction stakes place only in this porous media. The fluid and catalyst properties given in Section 4.1 are assumed to be uniform in all directions.

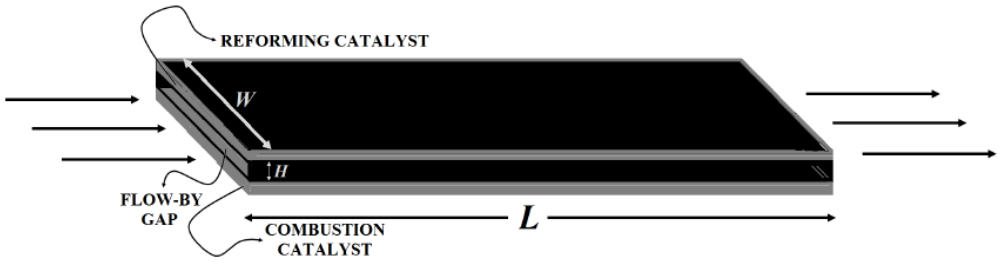

Figure 4.3. 3D representation of the microchannel reactor used in EGR of propane [31].

4.2.2. Working Equations

3D Navier-Stokes equations which are the partial differential equations (PDE) describing mass, momentum and energy conservation within the system, are used to simulate the EGR of propane in the catalytic microchannel shown in Figure 4.3. Solution of these equations gives the velocity, temperature, pressure and species concentration profiles in the channnel. All the physical properties (i.e., viscosity, diffusivity, thermal conductivity) are calculated by using the correlations given in the literature [36]. Rates and heats of reactions are introduced to the model as source terms in the species mass and energy equations. Momentum equations are modified in order to simulate the flow in the porous media.

4.2.2.1. Continuity Equation. The continuity equation in 3D cartesian coordinates is shown as Eq. 4.3.

$$\frac{\partial}{\partial x}\left(\rho_f v_x\right) + \frac{\partial}{\partial y}\left(\rho_f v_y\right) + \frac{\partial}{\partial z}\left(\rho_f v_z\right) = 0 \tag{4.3}$$

4.2.2.2. Momentum Conservation Equation. Conservation of momentum is valid for the channel where fluid flows and for the washcoat layers. The three dimensional Navier-Stokes equations in Cartesian coordinates for Newtonian fluids are solved to obtain momentum balances for fluid phase. The general form of this equation is:

$$\frac{\partial}{\partial t}\left(\rho_f \vec{\mathbf{v}}\right) + \nabla \cdot \left(\rho_f \vec{\mathbf{v}}\vec{\mathbf{v}}\right) = \vec{\mathbf{F}} - \nabla p + \nabla \cdot \bar{\bar{\tau}} + \rho_f \vec{g} \tag{4.4}$$

where the stress tensor $\bar{\bar{\tau}}$ is defined as:

$$\bar{\bar{\tau}} = \mu\left[\left(\nabla\vec{\mathbf{v}} + \nabla\vec{\mathbf{v}}^{\mathrm{T}}\right) - \frac{2}{3}\nabla \cdot \vec{\mathbf{v}}\mathbf{I}\right] \tag{4.5}$$

In Eq. 4.5 μ is the molecular viscosity of the gas mixture in channel, $\mathbf{I}$ is the unit tensor, and the second term on the right-hand side is the effect of volume dilation that contributes to dissipation of momentum due to viscous forces. Since its effect on the velocity field and the viscous heating of the fluid is small, it can be dropped out from the stress tensor term. Stress tensor inserted and simplified form of the momentum conservation equation in 3D Cartesian coordinates is given by Equations below;

$$\begin{aligned} &\frac{\partial}{\partial t}\left(\rho_f v_x\right) + v_x\frac{\partial}{\partial x}\left(\rho_f v_x\right) + v_y\frac{\partial}{\partial y}\left(\rho_f v_{xj}\right) + v_z\frac{\partial}{\partial z}\left(\rho_f v_x\right) \\ &= -\frac{\partial p}{\partial x} + \frac{\partial}{\partial x}\left(\mu\frac{\partial v_x}{\partial x}\right) + \frac{\partial}{\partial y}\left(\mu\frac{\partial v_x}{\partial y}\right) + \frac{\partial}{\partial z}\left(\mu\frac{\partial v_x}{\partial z}\right) \end{aligned} \tag{4.6}$$

$$\begin{aligned} &\frac{\partial}{\partial t}\left(\rho_f v_y\right) + v_x\frac{\partial}{\partial x}\left(\rho_f v_y\right) + v_y\frac{\partial}{\partial y}\left(\rho_f v_y\right) + v_z\frac{\partial}{\partial z}\left(\rho_f v_y\right) \\ &= -\frac{\partial p}{\partial y} + \frac{\partial}{\partial x}\left(\mu\frac{\partial v_y}{\partial x}\right) + \frac{\partial}{\partial y}\left(\mu\frac{\partial v_y}{\partial y}\right) + \frac{\partial}{\partial z}\left(\mu\frac{\partial v_y}{\partial y}\right) \end{aligned} \tag{4.7}$$

$$\begin{aligned} &\frac{\partial}{\partial t}\left(\rho_f v_z\right) + v_x\frac{\partial}{\partial x}\left(\rho_f v_z\right) + v_y\frac{\partial}{\partial y}\left(\rho_f v_z\right) + v_z\frac{\partial}{\partial z}\left(\rho_f v_z\right) \\ &= -\frac{\partial p}{\partial z} + \frac{\partial}{\partial x}\left(\mu\frac{\partial v_z}{\partial x}\right) + \frac{\partial}{\partial y}\left(\mu\frac{\partial v_z}{\partial y}\right) + \frac{\partial}{\partial z}\left(\mu\frac{\partial v_z}{\partial y}\right) \end{aligned} \tag{4.8}$$

In order to model the flow in porous media, a modified version of the momentum conservation equations which are known as Brinkman equations is needed in conventional calculation techniques. However by using FLUENT^{TM} 14.0 solution for the flow in porous media is obtained by an iterative procedure such as SIMPLE algorithm. In

the momentum equations given above, for each velocity component, the velocity field must satisfy the continuity equation Eq. 4.3 and also pressure gradient term has to be calculated but there is no specified equation for pressure. The necessary relation to calculate pressure cannot be obtained from density relation of pressure since the flow modeled in this work is incompressible which means density is constant. At his point SIMPLE algorithm solved the pressure-velocity coupling problem by using an iterative solution strategy. The working principle of SIMPLE algorithm can be summarized as [31, 42],

(i) set the boundary conditions and the initial guesses
(ii) compute the gradients of velocity and pressure
(iii) calculate coefficients of the equations and solve the discretized momentum equation to compute the intermediate velocity field
(iv) solve the pressure correction equation, and update velocity and pressure and any other scalars
(v) check for convergence; if not converged, store the computed values and go back to step (ii)

Momentum conservation equations are solved for the specific boundary conditions. Channel entrance is set to be a velocity inlet and normal inflow velocity ($v_z = U^{\text{in}}$) is specified at z = 0. For the gas-solid interface continuity of the velocity vector and continuity of the normal component of the momentum tensor is assumed. Channel exit is defined as the pressure outlet. All other boundaries are defined as the insulated walls. These expressions are summarized in Table 4.3.

Table 4.3. Boundary conditions used for momentum conservation equations.

Channel entrance	z = 0	$v_z = \mathrm{U}^{in}$
Gas-solid interface	0<z<L	$\vec{\mathbf{v}}\|_{\Gamma_{\text{gas}}} = \vec{\mathbf{v}}\|_{\Gamma_{\text{solid}}}$ $\vec{\mathbf{n}} \cdot \bar{\bar{\tau}}\|_{\Gamma_{\text{gas}}} = \vec{\mathbf{n}} \cdot \bar{\bar{\tau}}\|_{\Gamma_{\text{solid}}}$
Channel exit	z = L	$p = p^{\text{out}}$
All other boundaries	$\forall z$	$\vec{\mathbf{n}} \cdot \vec{\mathbf{v}} = 0$

4.2.2.3. Species Mass Conservation Equations. The general form of species mass conservation equation in 3D Cartesian coordinates is given as

$$\frac{\partial}{\partial t}\left(\rho_f Y_i\right) + \nabla \cdot \left(\rho_f \vec{\mathbf{v}} Y_i\right) = -\nabla \cdot \vec{J}_i + M_i \Re_{k_v}^{\mathrm{v}} + M_i \Re_{k_s}^{\mathrm{s}} A_s \tag{4.9}$$

In the above equation i is used to identify the species. $\vec{J}_i$ is the Fickian diffusive mass flux given by

$$\vec{J}_i = -\rho_f D_{\mathrm{eff},i,m} \nabla Y_i \tag{4.10}$$

where $D_{\mathrm{eff},i,m}$ is the effective diffusivity of species i in the mixture. Inserting the Fickian mass flux equation into Eq. 4.9 gives the species mass conservation equation in 3D Cartesian coordinates for this work:

$$\begin{aligned} &\frac{\partial}{\partial t}(\rho_f Y_i) + v_x \frac{\partial}{\partial x}(\rho_f Y_i) + v_y \frac{\partial}{\partial y}(\rho_f Y_i) + v_z \frac{\partial}{\partial z}(\rho_f Y_i) = \\ &\frac{\partial}{\partial x}[D_{\mathrm{eff},i,m} \frac{\partial}{\partial x}(\rho_f Y_i)] + \frac{\partial}{\partial y}[D_{\mathrm{eff},i,m} \frac{\partial}{\partial y}(\rho_f Y_i)] \\ &+ \frac{\partial}{\partial z}[D_{\mathrm{eff},i,m} \frac{\partial}{\partial z}(\rho_f Y_i)] + M_i \Re_{k_v}^{\mathrm{v}} + M_i \Re_{k_s}^{\mathrm{s}} A_s \end{aligned} \tag{4.11}$$

In Equations 4.10 and 4.11 $D_{\mathrm{eff},i,m}$ is the effective diffusivity of species i in the mixture. When the flow of gas phase mixture is under consideration, $D_{\mathrm{eff},i,m}$ simply equals $D_{i,m}$. For the flow in porous media this simplification cannot be done so that $D_{\mathrm{eff},i,m}$ is calculated by using $D_{i,m}$ and the Knudsen diffusion in the pores of the medium. In Eq. 4.11, $\Re_i^{\mathrm{v}}$ and $\Re_i^{\mathrm{s}}$ denotes the consumption or production rate of the

species i during volumetric and wall-surface reactions, respectively. Rate of reactions are calculated only within the catalytic washcoat, throughout the channel rate is zero. M_i is the molecular weight of species i, and A_s is the active surface area-to-volume ratio of the catalyst.

Species mass conservation equations are solved for the specific boundary conditions. In the channel entrance mass fraction of each species i assigned. For the gas-solid interface continuity of the mass fraction and continuity of the normal component of the diffusion tensor is assumed. In channel exit diffusive mass flux is defined to be zero. All other boundaries are defined as the insulated walls. These expressions are summarized in Table 4.4.

Table 4.4. Boundary conditions used for species mass conservation equations.

Channel entrance	z = 0	$Y_i = Y_i^{\text{in}}$
Gas-solid interface	0<z<L	$Y_i\|_{\Gamma_{\text{gas}}} = Y_i\|_{\Gamma_{\text{solid}}}$ $\vec{\mathbf{n}} \cdot (\vec{J_i} + \rho_f \vec{\mathbf{v}} Y_i)\|_{\Gamma_{\text{gas}}} =$ $\vec{\mathbf{n}} \cdot (\vec{J_i} + \rho_f \vec{\mathbf{v}} Y_i)\|_{\Gamma_{\text{solid}}}$
Channel exit	z = L	$\vec{\mathbf{n}} \cdot \vec{J_i} = 0$
All other boundaries	$\forall z$	$\vec{\mathbf{n}} \cdot (\vec{J_i} + \rho_f \vec{\mathbf{v}} Y_i) = 0$

4.2.2.4. Energy Equation. The general form of energy equation in 3D Cartesian coordinates is given as;

$$\epsilon \frac{\partial}{\partial t}(\rho_f c_{p_f} T) + (1-\epsilon)\frac{\partial}{\partial t}(\rho_s c_{p_s} T) + \nabla \cdot (\rho_f c_{p_f} \vec{\mathbf{v}} T)$$
$$= \nabla \cdot (k_{\text{eff}} \nabla T - \sum_i h_i \vec{J_i} + (\bar{\bar{\tau}} \vec{\mathbf{v}})) + \text{Q} \tag{4.12}$$

This generalized form is simplified by dropping out some terms due to their negligible effects on temperature profile in the channel. The term $\sum_i h_i \vec{J_i}$ which represents the heat transfer by the diffusive flux of all the species and the term $\bar{\bar{\tau}} \vec{\mathbf{v}}$ which represents

the heat exchange due to viscous dissipation have much less effect on the temperature variation of the system when compared to the term $\epsilon\frac{\partial}{\partial t}(\rho_f c_{p_f} T)$ which represents the conduction heat transfer, so they are dropped out. After these simplifications the energy equation in 3D Cartesian coordinates becomes

$$\begin{aligned}
&\epsilon\frac{\partial}{\partial t}(\rho_f c_{p_f} T) + (1-\epsilon)\frac{\partial}{\partial t}(\rho_s c_{p_s} T) + v_x\frac{\partial}{\partial y}(\rho_f c_{p_f} T) \\
&+v_y\frac{\partial}{\partial x}(\rho_f c_{p_f} T) + v_z\frac{\partial}{\partial z}(\rho_f c_{p_f} T) = \frac{\partial}{\partial x}[k_{\text{eff}}\frac{\partial}{\partial x}(\rho_f T)] \\
&+\frac{\partial}{\partial y}[k_{\text{eff}}\frac{\partial}{\partial y}(\rho_f T)] + \frac{\partial}{\partial z}[k_{\text{eff}}\frac{\partial}{\partial z}(\rho_f T)] + \text{Q}
\end{aligned} \tag{4.13}$$

Effective thermal conductivity, k_{eff} is calculated by taking the volume average of fluid (k_f) and solid (k_s) conductivities:

$$k_{\text{eff}} = \epsilon k_f + (1-\epsilon)k_s \tag{4.14}$$

Outside the porous media, when the flow of the gas phase is under consideration, the porosity ϵ is taken as 1 and Eq. 4.13 becomes,

$$\begin{aligned}
&\frac{\partial}{\partial t}(\rho_f c_{p_f} T) + v_x\frac{\partial}{\partial x}(\rho_f c_{p_f} T) + v_y\frac{\partial}{\partial y}(\rho_f c_{p_f} T) + v_z\frac{\partial}{\partial z}(\rho_f c_{p_f} T) \\
&= \frac{\partial}{\partial x}[k_f\frac{\partial}{\partial x}(\rho_f T)] + \frac{\partial}{\partial y}[k_f\frac{\partial}{\partial y}(\rho_f T)]\frac{\partial}{\partial z}[k_f\frac{\partial}{\partial z}(\rho_f T)] + \text{Q}
\end{aligned} \tag{4.15}$$

In these above equations the term Q represents the source of energy (heat gen-

erated or consumed) and it is calculated as;

$$\mathrm{Q} = \sum_{k_v=1}^{N_{\mathrm{vrxn}}} (-\Delta H_{k_v}) \mathcal{R}^{\mathrm{v}}_{k_v} + \sum_{k_s=1}^{N_{\mathrm{srxn}}} (-\Delta H_{k_s}) A_s \mathcal{R}^{\mathrm{s}}_{k_s} \tag{4.16}$$

Energy equations are solved for the specific boundary conditions. In the channel entrance constant inlet temperature is defined. For the gas-solid interface continuity of temperature and continuity of the normal component of the heat diffusion tensor is assumed. In channel exit diffusive heat flux is defined to be zero. All other boundaries are defined as the insulated walls. These expressions can be summarized as;

Table 4.5. Boundary conditions used for energy equation.

Channel entrance	z = 0	$T_i = T_i^{\mathrm{in}}$
Gas-solid interface	0<z<L	$T_i\|_{\Gamma_{\mathrm{gas}}} = T_i\|_{\Gamma_{\mathrm{solid}}}$ $\vec{\mathbf{n}} \cdot (-k_{\mathrm{eff}} \nabla T + \rho_f c_{p_f} \vec{\mathbf{v}} T)\|_{\Gamma_{\mathrm{gas}}} =$ $\vec{\mathbf{n}} \cdot (-k_{\mathrm{eff}} \nabla T + \rho_f c_{p_f} \vec{\mathbf{v}} T)\|_{\Gamma_{\mathrm{solid}}}$
Channel exit	z = L	$\vec{\mathbf{n}} \cdot (-k_{\mathrm{eff}} \nabla T) = 0$
All other boundaries	$\forall z$	$\vec{\mathbf{n}} \cdot (-k_{\mathrm{eff}} \nabla T + \rho_f c_{p_f} \vec{\mathbf{v}} T) = 0$

4.2.3. Reaction Kinetics

The kinetic expressions for the SR reaction of propane is obtained from Li *et al.* [35]. The detailed expressions for the rate of the SR reaction occurring on 2wt% Rh/δ-Al_2O_3 coated catalytic layers in microchannel are given by Equations 4.17 and 4.18 and the necessary kinetic parameters are tabulated in Table 4.7.

$$\mathcal{R}^{\mathrm{v}}_{SR} = \frac{\mathrm{k_{sr} K_1 P_{C_3H_8} K_2 P_{H_2O}}}{(1 + \mathrm{K_1 P_{C_3H_8}} + K_2 \mathrm{P_{H_2O}})^2} \tag{4.17}$$

$$k_{\mathrm{SR}} = \mathrm{A}\exp(-\frac{\mathrm{E}_a}{\mathrm{RT}}) \tag{4.18}$$

Table 4.6. Kinetic parameters for SR rate equation (Langmuir-Hinshelwood model).

K_1	13.3 atm^{-1}
K_2	0.94 atm^{-1}
k	1.18 mmol g^{-1} s^{-1}
A	7.5×10^4 mmol g^{-1} s^{-1}
$\mathrm{E_a}$	68.8 kJ mol^{-1}

The kinetic expressions for the TOX reaction of propane is obtained from Kaisare *et al.* [24]. The total kinetic scheme for the rate of the TOX reaction occurring on 0.2wt% Pt/δ-$\mathrm{Al_2O_3}$ coated catalytic layers in microchannel is given below.

$$\mathcal{R}^{\mathrm{s}}_{TOX} = \frac{\mathrm{k}^{\mathrm{ads}}_{\mathrm{C_3H_8}}\mathrm{C}_{\mathrm{s,C_3H_8}}}{\left(1+\sqrt{\mathrm{k}^{\mathrm{ads}}_{\mathrm{O_2}}\mathrm{C}_{\mathrm{s,O_2}}/\mathrm{k}^{\mathrm{des}}_{\mathrm{O_2}}}\right)^2} \tag{4.19}$$

$$k^{\mathrm{ads}}_{\mathrm{k}} = \frac{s_0}{\Gamma}\sqrt{\frac{\mathrm{RT}}{2\pi M_{\mathrm{k}}}}\left(\frac{\mathrm{T}}{\mathrm{T}_{\mathrm{ref}}}\right)^{\beta^{ads}_{\mathrm{k}}}\left(-\frac{\mathrm{E}^{ads}_{\mathrm{a,k}}}{\mathrm{RT}}\right) \tag{4.20}$$

$$k^{\mathrm{des}}_{\mathrm{k}} = \mathrm{A}\left(\frac{\mathrm{T}}{\mathrm{T}_{\mathrm{ref}}}\right)^{\beta^{des}_{\mathrm{k}}}\left(-\frac{\mathrm{E}^{des}_{\mathrm{a,k}}}{\mathrm{RT}}\right) \tag{4.21}$$

The kinetic constants needed to evaluate the rate is given in Table 4.7. It has to be mentioned that the reference temperature T_{ref} is given as 300K and the value of the site density Γ is 2.5×10^{-9}.

Table 4.7. Kinetic rate constants for propane combustion.

	A (s^{-1}) or s_0	β	E_a (kcal/mol)
C_3H_8 adsorption	0.06	0.154	4
O_2 adsorption	0.0542	0.766	0
O_2 desorption	8.41×10^12	0.766	Eq.4.22

$$\mathrm{E}_{\mathrm{a,O_2}}^{des} = 52.8 - 2.3(\mathrm{T}/300) - 32.0\theta_{O*} \tag{4.22}$$

$$\theta_{O*} = 1 - \frac{1}{\left(1 + \sqrt{\mathrm{k}_{\mathrm{O_2}}^{\mathrm{ads}} \mathrm{C}_{\mathrm{s,O_2}} / \mathrm{k}_{\mathrm{O_2}}^{\mathrm{des}}}\right)^2} \tag{4.23}$$

4.2.4. Physical Properties

In this section the calculation procedure of the physical properties of the fluid mixtures, catalytic washcoats and the walls will be explained. These properties are needed in order to solve the transport equations. The reacting fluid mixture consists of propane, steam, carbon dioxide, carbon monoxide, hydrogen, nitrogen and oxygen. Fluid viscosity for the mixture is calculated by [37]:

$$\mu = \sum_{i=1}^{N_g} \frac{x_i \mu_i}{\sum_{l=1}^{N_g} x_{il} \Phi_{il}}, \qquad l \neq i \tag{4.24}$$

with

$$\Phi_{il} = \frac{1}{\sqrt{8}} \left(1 + \frac{M_i}{M_l}\right)^{-1/2} \left[1 + \left(\frac{\mu_i}{\mu_l}\right)^{1/2} \left(\frac{M_l}{M_i}\right)^{1/4}\right]^2$$

i and l are the species indices where $i, l = 1, 2, \ldots, N_g$.

Dynamic viscosity of each species i in microchannel is calculated by [38]:

$$\mu_i = 2.6693 \times 10^{-6} \frac{\sqrt{10^3 M_i T_i}}{\varpi_i^2 \Omega_i} \tag{4.25}$$

where ϖ_i is the collision diameter and Ω_i is the collision integral which are obtained from [38].

Thermal conductivity of the gaseous mixture in microchannel is calculated by [39]

$$k_f = \sum_{i=1}^{N_g} \frac{x_i k_i}{\sum_{l=1}^{N_g} x_{il} \Phi_{il}}, \qquad l \neq i \tag{4.26}$$

k_i, is obtained from [38]

$$k_i = 8.3224 \times 10^{-4} \frac{\sqrt{10^{-3} T / M_i}}{\varpi_i^2 \Omega_i} \tag{4.27}$$

Diffusivity of each species i in the mixture is calculated by [39]:

$$D_{i,m} = \frac{1 - Y_i}{\sum_{l=1}^{N_g} Y_i / D_{il}}, \qquad l \neq i \tag{4.28}$$

The effective diffusivity, $D_{\text{eff},i,m}$, in the porous catalyst washcoats are calculated

from [40]

$$D_{\text{eff},i,m} = \frac{\epsilon_{\text{cat}}}{\tau_{\text{cat}}} \left[\frac{1}{D_{K,i}} + \frac{1}{D_{i,m}} \right]^{-1} \tag{4.29}$$

where $D_{K,i}$ is the Knudsen diffusivity which is a function of the average pore diameter d_{pore}, molecular weight of the species and the temperature [40]:

$$D_{K,i} = 48.5 d_{\text{pore}} \sqrt{\frac{T}{M_i}} \tag{4.30}$$

Density of the gaseous mixtures are calculated using Eq. 4.31, assuming they behave ideally under atmospheric pressure and high temperatures:

$$\rho_f = \frac{p^{\text{in}} M}{R T^{\text{in}}} \tag{4.31}$$

The heat generated in the catalyst layer is calculated via molar enthalpies of species involved in the reactions as shown in Eq. 4.16. Enthalpy of the reaction is simply calculated by subtracting the enthalpy of the reactants from products;

$$\Delta H_{rxn} = \sum \sigma_i (\Delta H_i) \tag{4.32}$$

where σ is the stoichiometric coefficient of the species in the reaction and subscript denotes either the surface or volumetric reaction. For each species i, the molar enthalpy

is calculated at a specific temperature by using;

$$\Delta H_i = \Delta H_{i,ref} + \int_{T_{ref}}^{T} c_{p,i} dT \tag{4.33}$$

where the term $c_{p,i}$ is the heat capacity of each species and calculated by;

$$c_{p,i} = A + BT + CT^2 + DT^3 \tag{4.34}$$

5. RESULTS AND DISCUSSION

5.1. CFD Simulation of Exhaust Gas Reforming of Propane in a Heat Exchange Integrated Microchannel Reactor

Exhaust gas reforming of propane is simulated in a microchannel which involves TOX and SR reactions happening successively. The effect of amount of propane and steam injected to the reformer, and total flow rate on temperature and product distribution through the channel is investigated in different exhaust gas compositions from diesel and gasoline ICEs.

5.1.1. Effect of Oxygen-to-Carbon Ratio for Gasoline-Fueled ICEs

A typical simulation of the temperature distribution obtained in the heat-exchange integrated catalytic microchannel is given in Figure 5.1. As the ICE effluent and propane enters to the reformer at the conditions given under Case 2 (Table 4.1), TOX is triggered immediately and continues to raise the temperature over the Pt layer up to 1802.6 K until the oxygen in the feed is consumed completely. This exothermal heat is then utilized by endothermic SR which reduces temperature down to 1597.2 K at the channel exit. The unified temperature distribution at the downstream clearly demonstrates that exothermal heat is effectively distributed along the channel length without a remarkable hot-spot formation.

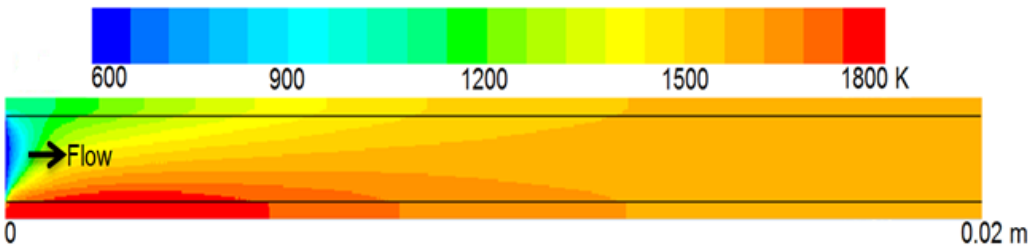

Figure 5.1. 2D plot of temperature profile obtained for Case 2 (Table 4.1)in a catalytic microchannel (Rh/δ-Al_2O_3(top layer); Pt/δ-Al_2O_3(bottom layer)).

This characteristic response of the microchannel reactor is also observed for TOX/SR coupling of propane at other O_2/C ratios of a gasoline ICE, whose results are given in Table 5.1 and in Figure 5.1, with the latter showing centerline temperature distributions. The results show that centerline temperature is almost uniform along the second half of the channel length. Uniformity of temperature distribution, a property essential for high reforming efficiencies, is clearly better than that reported for packed bed and monolith reactors, which are typically characterized by a notable hot spot followed by a fast temperature drop [9,16]. Even though it is operated at a GHSV of 2.2×10^4 h^{-1}, the differences between maximum temperature and exit temperature in the microchannel reactor are found to be less than 200 K (Table 5.1), whereas the values are notably higher than ∼200 K for packed bed and monolith reactors operated at GHSVs (based on catalyst volume) in excess of 1×10^5 h^{-1} [9,16]. Considering the fact that high GHSV operations will lead to slower temperature drops after the hot-spot formation [16], microchannel reactor, which is operated at a ∼5 times smaller GHSV, gave much smaller gradients between the maximum and exit temperatures.

Table 5.1. Volumetric product compositions (given in dry basis), maximum channel (T_{max}) and difference between maximum and exit channel temperatures ($\Delta T = T_{max}$-T_{exit}) while comparing O_2/C ratio. See Table 4.1 for other operating conditions.

Case	**O_2/C**	**H_2 %**	**CO %**	**CO_2 %**	**T_{max} (K)**	**$\Delta T = T_{max} - T_{exit}$**
1	0.07	4.50	2.37	16.07	1303.2	88.2
2	0.45	13.50	6.15	17.47	1802.6	205.4
3	0.46	21.19	9.45	16.46	2224.2	273.9

It can also be noted that uniform temperature distribution is provided even if engine is operating at extreme cases such as at low load (Case 1) or high load (Case 3) (Table 5.1, Figure 5.1). Even though the microchannel length can be quite small (2×10^{-2} m) for use as an exhaust gas reformer, temperature distribution at the downstream part of a longer (e.g. 1×10^{-1} m) reactor will most likely to be the same as shown in Figure 5.1, which indicates a stable uniformity in the last ∼35% of the volume. These findings show that microchannel reactor has inherently better heat transfer characteristics which make it flexible in terms of handling wide range of space velocities existing in a typical vehicular operation.

The dry-basis concentrations of the products (H_2, CO, CO_2), defined as the ratio of the number of moles of the pertinent species to the total number of moles of all species in the product stream excluding steam, are also provided in Table 5.1. The trends can be explained by the amount of propane injected into the reformer. Among the three cases, Case 1 involves the consumption of the lowest quantity of propane (2% by volume). As a result, less fuel is oxidized to give a maximum temperature of 1303.2 K, and less heat is released to run endothermic SR to produce quantities of H_2 and CO lower than estimated for Cases 2 and 3, which involves the use of higher quantities of propane, namely 5% and 8%, respectively.

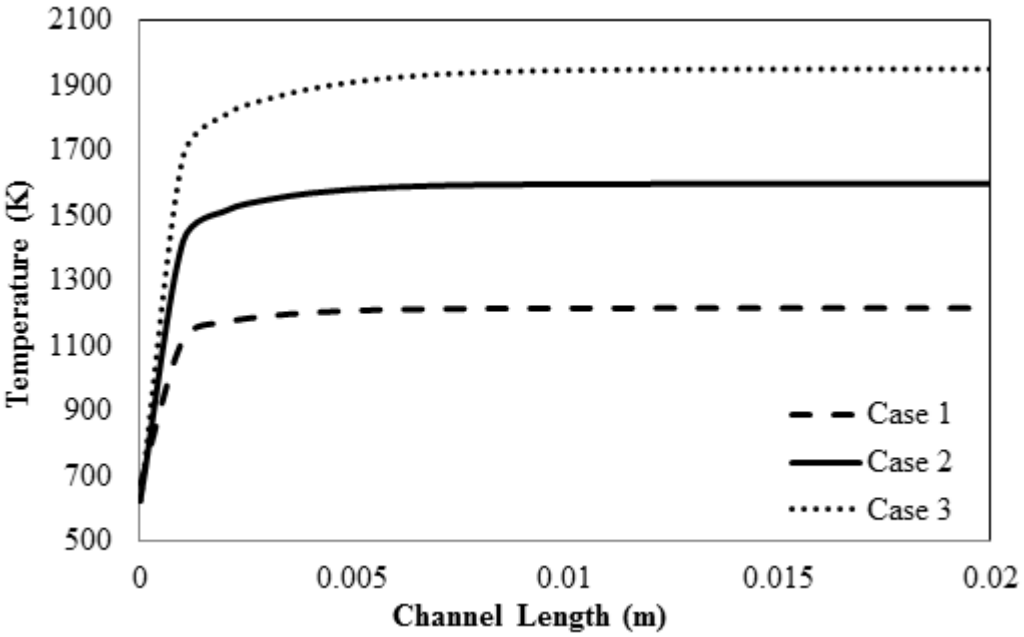

Figure 5.2. Centerline temperature profiles from the reforming of gasoline-fueled ICE exhaust gas with propane.

5.1.2. Effect of Total Flow Rate for Gasoline-Fueled ICEs

Sensitivity of temperature and product distribution in the microchannel EGR unit against the effects of total feed flow rate is investigated and reported in Table 5.2 and in Figure 5.4.

Although the EGR feed compositions are kept constant (Table 4.1), change in the

Table 5.2. Volumetric product compositions (given in dry basis), maximum channel temperature (T_{max})and difference between maximum and exit channel temperatures ($\Delta T = T_{max}$-T_{exit}) while comparing total flow rates. See Table 4.1 for other operating conditions.

Case	$\mathbf{v^*_{total}}$ **(Nml/min)**	$\mathbf{H_2}$ **%**	**CO CO %**	$\mathbf{CO_2}$ **%**	$\mathbf{T}_{max}$ **(K)**	$\mathbf{\Delta T = T_{max} - T_{exit}}$
2	43.75	13.50	6.15	17.47	1802.6	205.4
2a	21.88	11.16	5.74	18.12	1597.7	186.5
2b	87.50	14.27	6.30	17.50	1966.2	176.7
2c	131.25	13.84	6.12	17.57	2022.9	175.9

total feed flow rate corresponds to respective variations in the flow rate of the reactive components. The centerline temperatures (Figure5.4) show that, by increasing the total flow rate, magnitude of the exit temperature increases and the location where profile becomes flat moves in the direction of channel length (i.e. towards the channel exit).

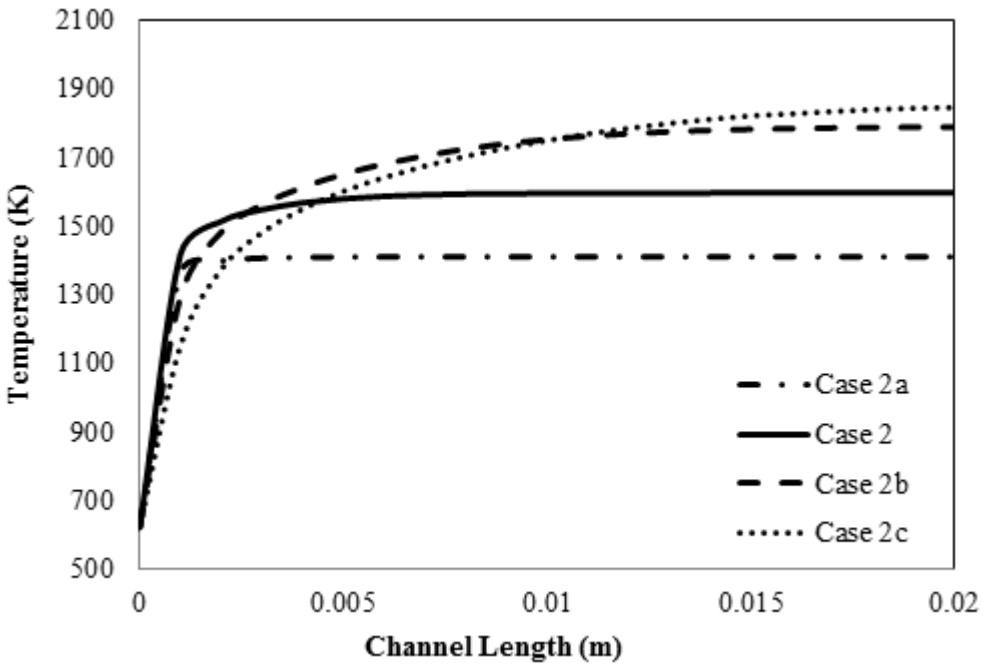

Figure 5.3. Effect of total feed flow rate on centerline temperature profiles from the reforming of gasoline-fueled ICE exhaust gas with propane.

Increasing the total flow rate corresponds to the release of higher exothermal heat

due to TOX of more propane. The end effect is higher channel temperatures, followed by improved H_2 and CO compositions (Table 4.1; Cases 2a, 2 and 2b). However this condition leads to increase in GHSV which spreads the exothermal heat and shifts the steady-temperature zone further downstream of the catalyst bed. In Case 2c, where GHSV is the highest (6.6×10^4 h^{-1}), H_2 and CO compositions are found to decrease. It can be claimed that when GHSV is changed from 4.4×10^4 h^{-1} (Case 2b) to 6.6×10^4 h^{-1} (Case 2c), reactive fluid resides shortly on the catalyst bed to produce lower H_2 and CO compositions. It can also be noted that increased feed flow rates lead to better heat dissipation along the reactor volume and reduce the differences between maximum and exit temperatures (Table 5.2).

5.1.3. Effect of Steam-to-Carbon Ratio for Gasoline-Fueled ICEs

The effects of extra steam injection to the EGR feed, expressed in terms of molar steam to molar carbon atom ratio (H_2O/C), on temperature and product distribution are shown in Table 5.3 and in Figure 5.5. Note that the total flow rate is kept constant at 43.75 ml/min by changing the N_2 flow rate accordingly. Extra steam addition is found to improve H_2 and CO compositions due to favored SR chemistry (Table 5.3). On the other hand, decrease in channel temperature due to the increased endothermicity of the steam-driven SR is observed Figure5.5. Since total flow rate is kept constant, the length of the flat zones of the temperature profiles remained unchanged.

Table 5.3. Volumetric product compositions (given in dry basis), maximum channel temperature (T_{max})and difference between maximum and exit channel temperatures ($\Delta T = T_{max}$-T_{exit}) while comparing H_2O/C ratio. See Table 4.1 for other operating conditions.

Case	**H_2O/C**	**H_2 %**	**CO %**	**CO_2 %**	**T_{max} (K)**	**$\Delta T = T_{max} - T_{exit}$**
2	0.55	13.50	6.15	17.47	1802.6	205.4
2d	0.28	12.50	5.64	17.29	1857.0	192.7
2e	1.11	15.27	7.00	18.46	1744.7	218.3
2f	1.66	17.03	7.84	19.95	1711.0	224.1

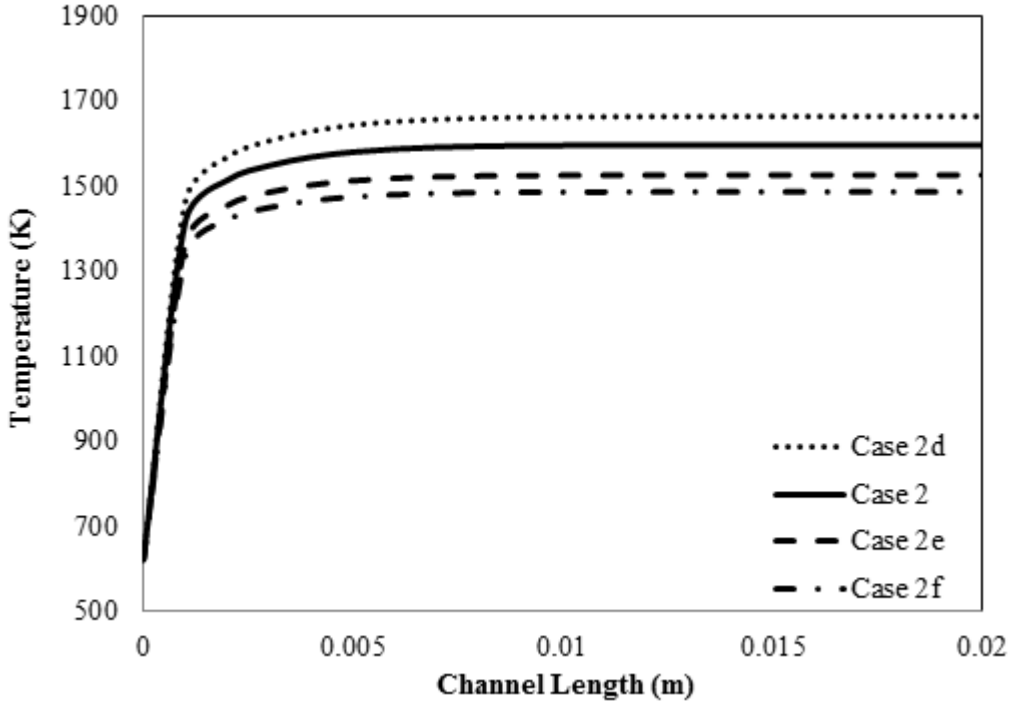

Figure 5.4. Effect of H_2O/C ratio on centerline temperature profiles from the reforming of gasoline-fueled ICE exhaust gas with propane.

5.1.4. Parametric Study for Diesel-Fueled ICEs

The outputs of a diesel-driven ICE are also simulated in a microchannel EGR process and the respective results are given in Table 5.4 and in Figure5.5.

Table 5.4. Volumetric product compositions (given in dry basis), maximum channel temperature (T_{max})and difference between maximum and exit channel temperatures ($\Delta T = T_{max}$-T_{exit}) for diesel ICE effluent. See Table 4.1 for other operating conditions.

Case	**H_2 %**	**CO %**	**CO_2 %**	**T_{max} (K)**	**$\Delta T = T_{max} - T_{exit}$**
4	13.10	5.81	14.45	1832.2	198.8
5	12.44	5.48	13.28	1813.7	199.4
6	11.94	5.24	12.81	1801.2	189.3
7	11.54	5.05	11.99	1795.4	185.7

It can be observed that, although the feed temperatures vary in the 473-643 K range, centerline temperature profiles turn out to be close to each other, and the difference in the exit temperatures becomes less than ∼50 K (Figure 5.6). Although

Case 7 (air/fuel=4.25) is fed at 473 K, high O_2 content (15.8%) in the feed allows increased TOX conversions and subsequent release of exothermal heat that brings the exit temperature close to that of Case 4 fed at 643 K, but with the lowest O_2 content of 9.1%. H_2 and CO compositions given in Table 5.4 are in accordance with channel temperatures and H_2O quantities in the feed, both of which favor endothermic SR conversion; highest yields are obtained in Case 4 fed with 6.2% of H_2O and gave the highest channel temperature (Figure 5.6). Comparison of reforming of gasoline and diesel ICE exhaust gas compositions with the same amount of propane (5%; Case 2 vs. Cases 4-7) shows that, H_2 and (increase in) CO compositions are slightly higher in Case 2. This is because of the fact that compared to that of gasoline, diesel exhaust gas stream is rich with O_2, leading to increased propane consumption in TOX and use of less propane in SR.

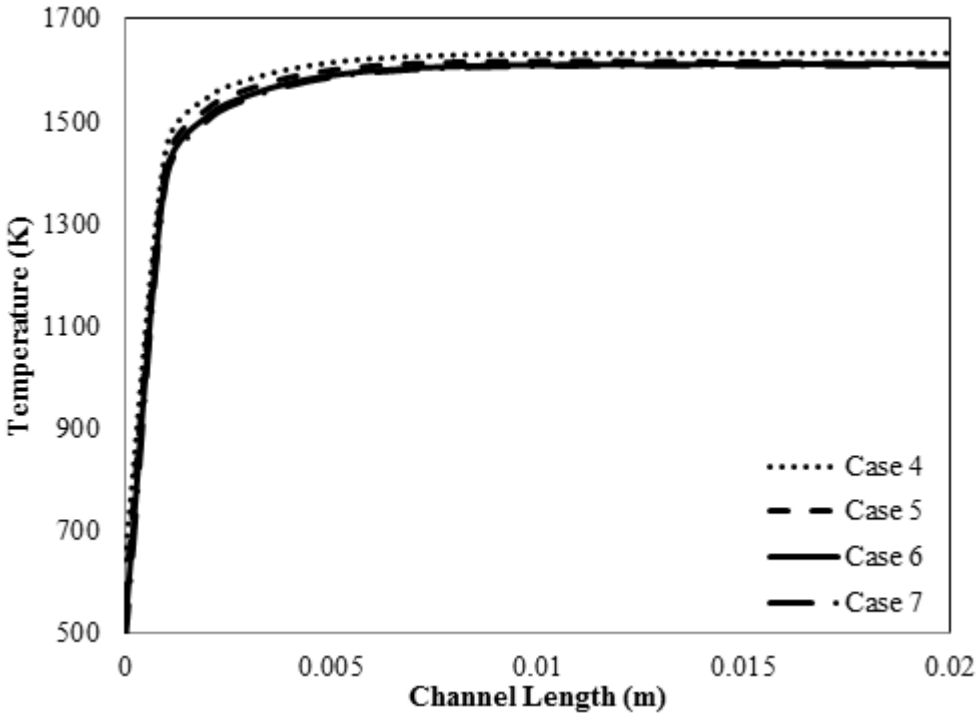

Figure 5.5. Centerline temperature profiles from the reforming of diesel-fuelled ICE exhaust gas with propane.

5.2. Oxidative Steam Reforming of Methane in a Catalytic Microchannel Reactor under EGR Conditions

The major aim of this study is to investigate the effects of operating conditions (temperature, H_2O/C and O_2/C rations in the feed), and of different catalysts (0.2wt%Pt-2wt%Rh, 2%Pt-2%Rh and 2%Rh-2%Rh) coated on two different sides of the microchannel reactor (Figure 3.3) on methane conversion and product distribution during OSR of methane in the context of EGR. These experiments are conducted at 873, 923 and 973K at atmospheric pressure with H_2O/C ratios of 1, 1.25 and 1.5, and O_2/C ratios of 0.5, 0.75 and 1. H_2O/C ratio is defined as the number of moles of steam divided by that of methane at the inlet. O_2/C ratio is defined as the number of moles of oxygen divided by that of methane at the inlet.

5.2.1. Methane Conversion

To understand the effect of temperature on methane conversion experiments are conducted for operating conditions given in Table 3.5. Feed compositions and flow rates are arranged as explained in Section 3.4.2, Table 3.6. The results are given in Figures 5.6 - 5.10. Regardless of the catalyst used in the experiments methane conversion increases with increasing temperature. The highest increase in conversion is observed when 0.2%Pt-2%Rh catalyst is used, the conversion is increased from 7% to 18% with the increase in temperature from 600 to 700°C. When 0.2%Pt-2%Rh and 2%Pt-2%Rh combinations are compared, even Pt loading is increased 10-fold in the latter such important increase is not observed in methane conversion. This can be explained by the fact that increasing metal loading decreases the dispersion of the active sites. In the case where 0.2%Pt is loaded dispersion is better and it gives methane conversions compatible with 2%Pt loaded one [43, 44]. 2%Pt-2%Rh and 2%Rh-2%Rh deliver similar methane conversions only differ from each other approximately 5%. According to the performance of catalyst combinations on methane conversion, a placement like 2%Rh-2%Rh > 2%Pt-2%Rh > 0.2%Pt-2%Rh is obtained. Since 2%Rh-2%Rh and 2%Pt-2%Rh have higher metal loadings than 0.2%Pt-2%Rh, they are expected to give more conversion. And since Rh is a better SR catalyst than PT [29] and its com-

bustion performance is also very good [26], observing more methane conversion over 2%Rh-2%Rh than 2%Pt-2%Rh is very logical.

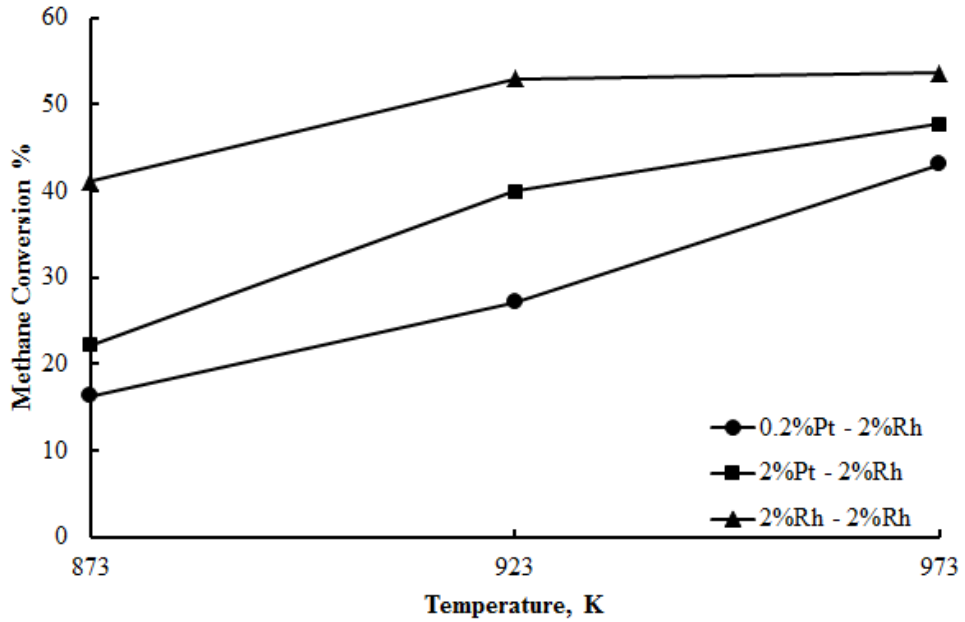

Figure 5.6. Effect of temperature on methane conversion over 0.2wt%Pt-2wt%Rh, 2%Pt-2%Rh and 2%Rh-2%Rh ($H_2O/C = 1$, $O_2/C = 1$).

In order to understand the effect of H_2O/C ratio on methane conversion over 0.2wt%Pt-2wt%Rh, 2%Pt-2%Rh and 2%Rh-2%Rh catalyst combinations the experiments are conducted according to the operating conditions given in Table 3.5. Feed compositions and flow rates are arranged as explained in Section 3.4.2 and in Table 3.6. The results are given in Figures 5.11-5.13. When the obtained plots are analyzed, the same trend is observed in all figures which shows that methane conversion increases with increasing H_2O/C ratio. Conversion increases by 4% when 0.2wt%Pt-2wt%Rh and 2%Pt-2%Rh catalysts are used and 7% when 2%Rh-2%Rh is used as H_2O/C ratio goes from 1 to 1.5. Since these values are quite small, it can be said that increasing H_2O/C ratio does not increase methane conversion significantly. Methane amount is fixed and limited for each experiment, and it is known that in OSR the reactions occur in the order of first TOX and then SR [3], so no matter how much the amount of steam in the feed stream increases, there is always similar amount of methane left for SR after TOX occurred. Therefore, it is very normal not to observe big changes in

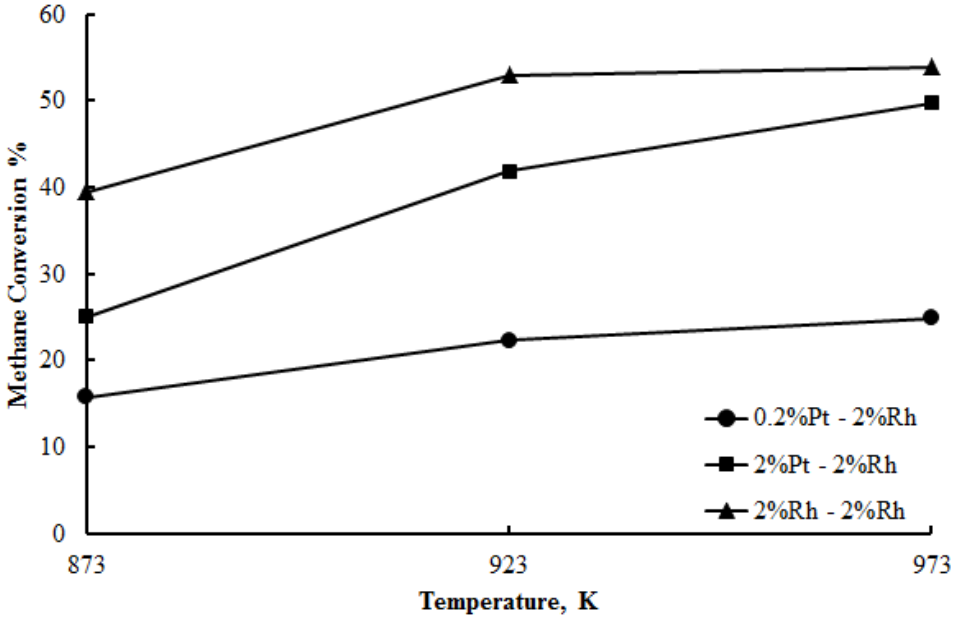

Figure 5.7. Effect of temperature on methane conversion over 0.2wt%Pt-2wt%Rh, 2%Pt-2%Rh and 2%Rh-2%Rh ($H_2O/C = 1.25$, $O_2/C = 1$).

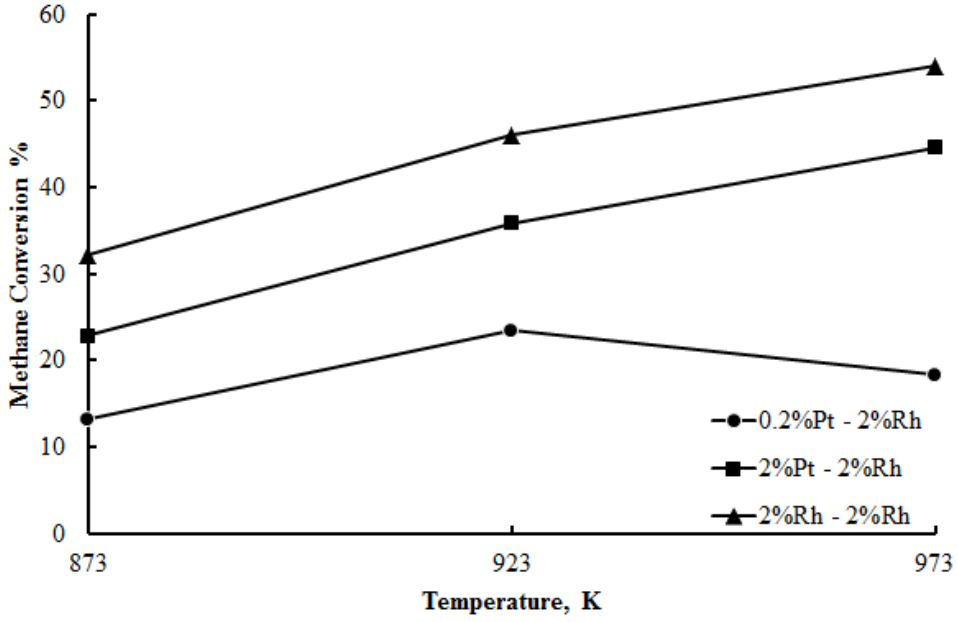

Figure 5.8. Effect of temperature on methane conversion over 0.2wt%Pt-2wt%Rh, 2%Pt-2%Rh and 2%Rh-2%Rh ($H_2O/C = 1.5$, $O_2/C = 1$).

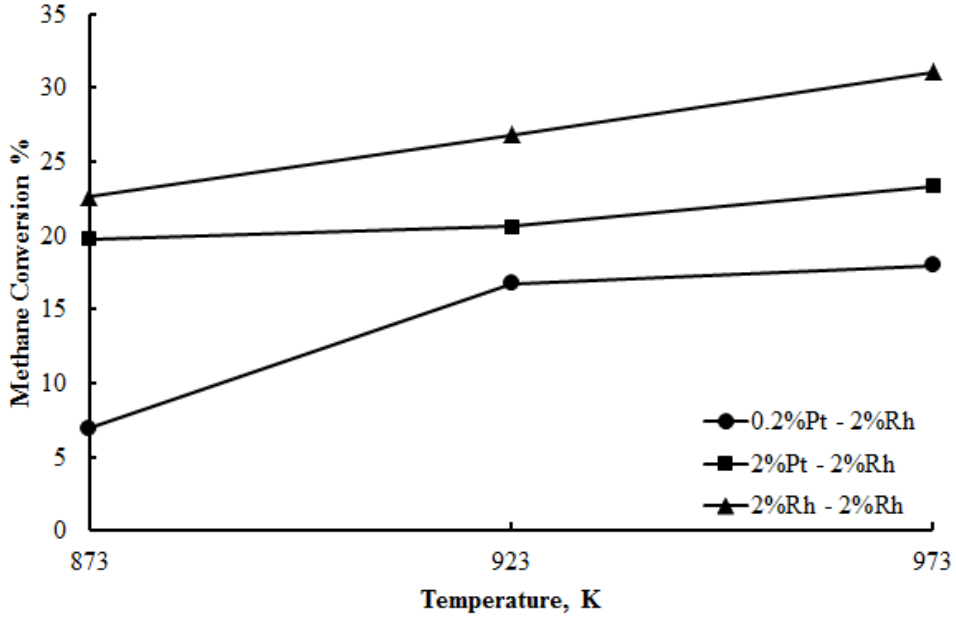

Figure 5.9. Effect of temperature on methane conversion over 0.2wt%Pt-2wt%Rh, 2%Pt-2%Rh and 2%Rh-2%Rh ($H_2O/C = 1.5$, $O_2/C = 0.5$).

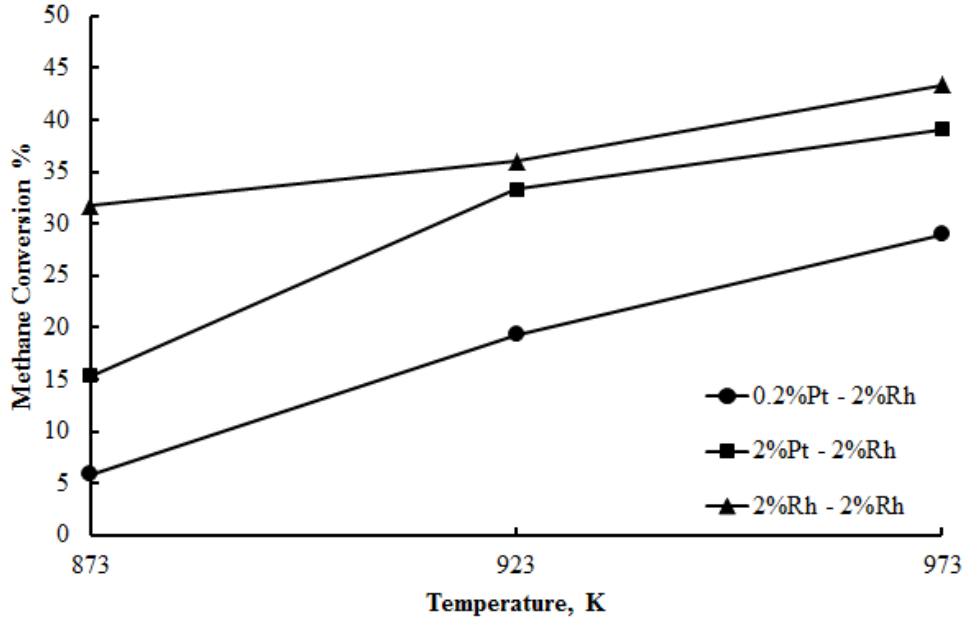

Figure 5.10. Effect of temperature on methane conversion over 0.2wt%Pt-2wt%Rh, 2%Pt-2%Rh and 2%Rh-2%Rh ($H_2O/C = 1.5$, $O_2/C = 0.75$).

methane conversion as H_2O/C ratio increases.

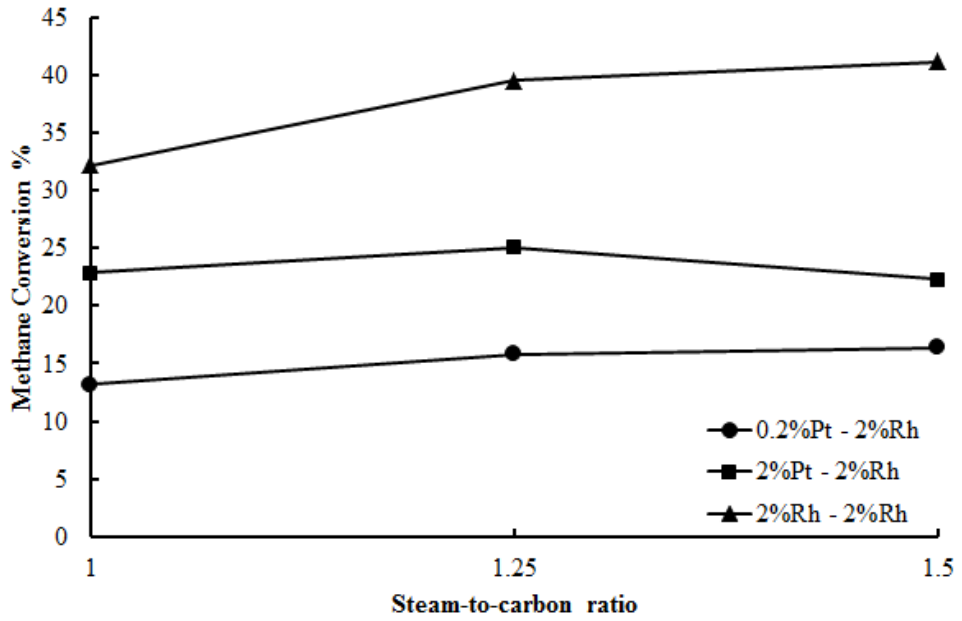

Figure 5.11. Effect of H_2O/C ratio on methane conversion over 0.2wt%Pt-2wt%Rh, 2%Pt-2%Rh and 2%Rh-2%Rh (T = 600°C, O_2/C = 1).

Figures 5.14-5.16 show the results obtained to show the effect of O_2/C ratio on methane conversion over 0.2wt%Pt-2wt%Rh, 2%Pt-2%Rh and 2%Rh-2%Rh catalyst combinations. It is observed that methane conversion increases with increasing O_2/C ratio for all catalyst combinations studied. As opposed to the previous situation where H_2O/C ratio is changed, significant improvements in methane conversion is observed upon changing O_2/C ratio. Increasing the partial pressure of O_2 in the feed stream favors TOX so that the amount of H_2O produced is increased which triggers SR, and both TOX and SR conversions are increased. The highest methane conversion achieved is 27% for the case of 0.2%Pt-2%Rh whereas 40% conversion is achieved for 2%Pt-2%Rh and 53% for 2%Rh-2%Rh, which can be explained by the increase in the active metal loadings for the latter ones. Also when 2%Pt-2%Rh and 2%Rh-2%Rh are compared, the latter gives better results. This situation is valid for all experiments conducted, in all those runs it is seen that highest conversion values are achieved over 2%Rh-2%Rh. In a methane limited environment with the fact that TOX happening before SR, it can be said that Rh is a very good combustion catalyst and probably better than Pt.

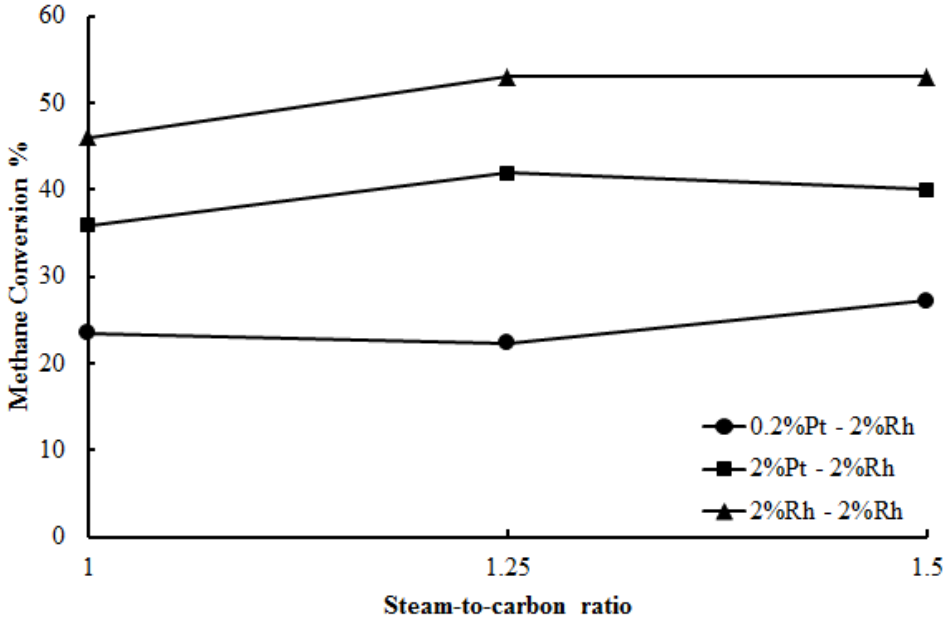

Figure 5.12. Effect of H_2O/C ratio on methane conversion over 0.2wt%Pt-2wt%Rh, 2%Pt-2%Rh and 2%Rh-2%Rh (T = 650°C and $O_2/C = 1$).

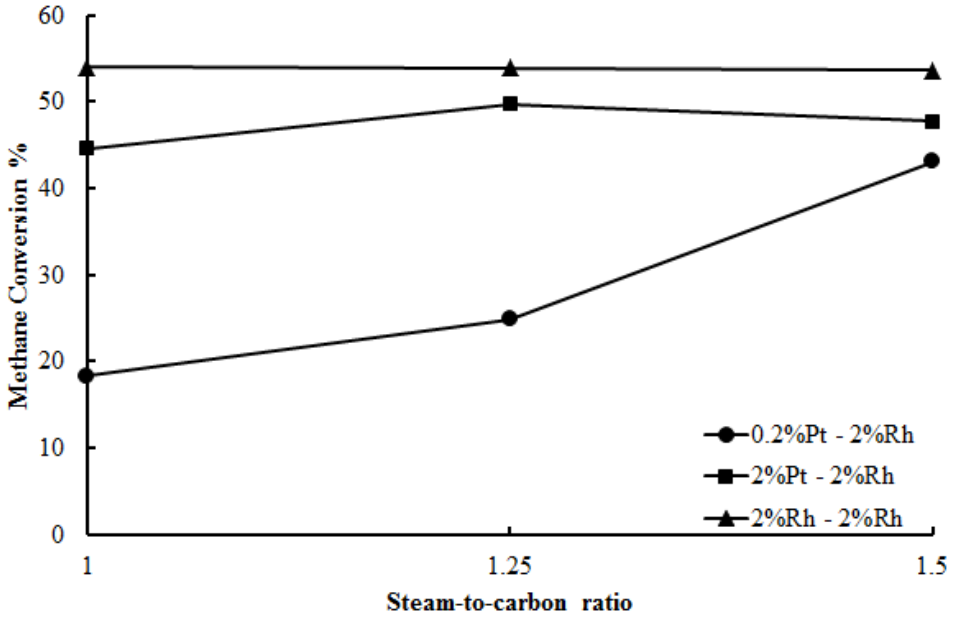

Figure 5.13. Effect of H_2O/C ratio on methane conversion over 0.2wt%Pt-2wt%Rh, 2%Pt-2%Rh and 2%Rh-2%Rh (T = 700°C, $O_2/C = 1$).

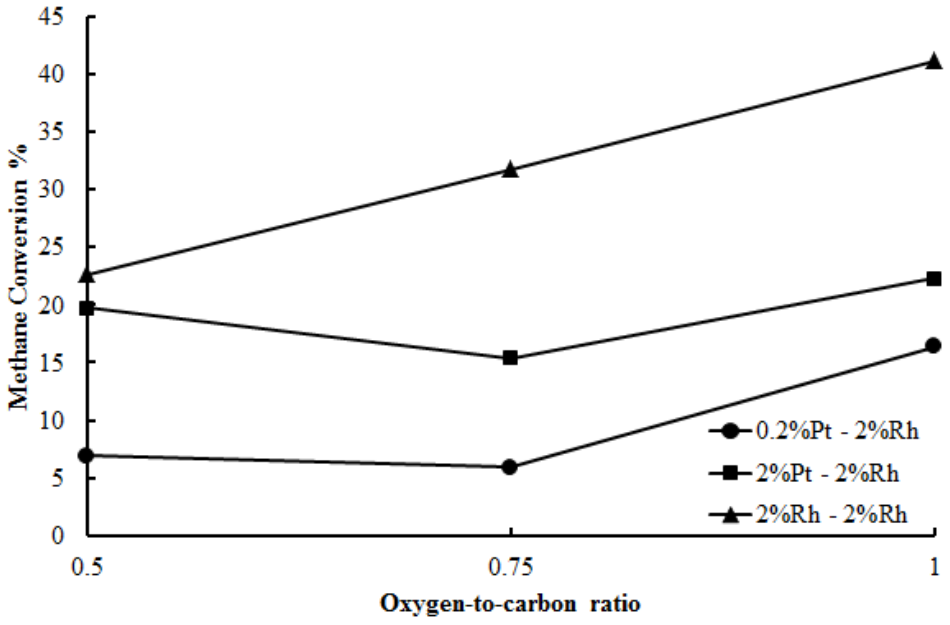

Figure 5.14. Effect of O_2/C ratio on methane conversion over 0.2wt%Pt-2wt%Rh, 2%Pt-2%Rh and 2%Rh-2%Rh (T = 600°C, H_2O/C = 1.5).

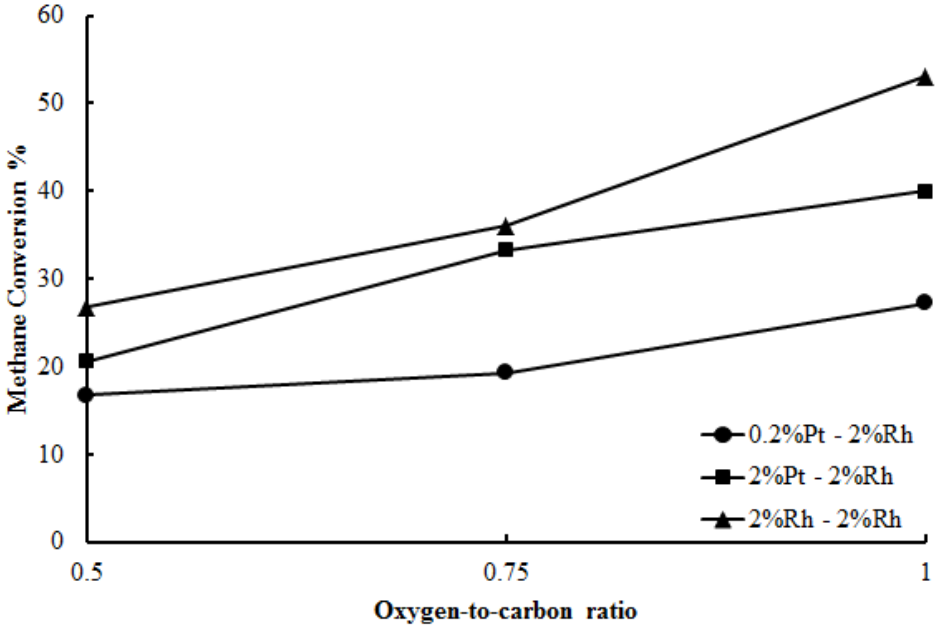

Figure 5.15. Effect of O_2/C ratio on methane conversion over 0.2wt%Pt-2wt%Rh, 2%Pt-2%Rh and 2%Rh-2%Rh (T = 650°C and H_2O/C = 1.5).

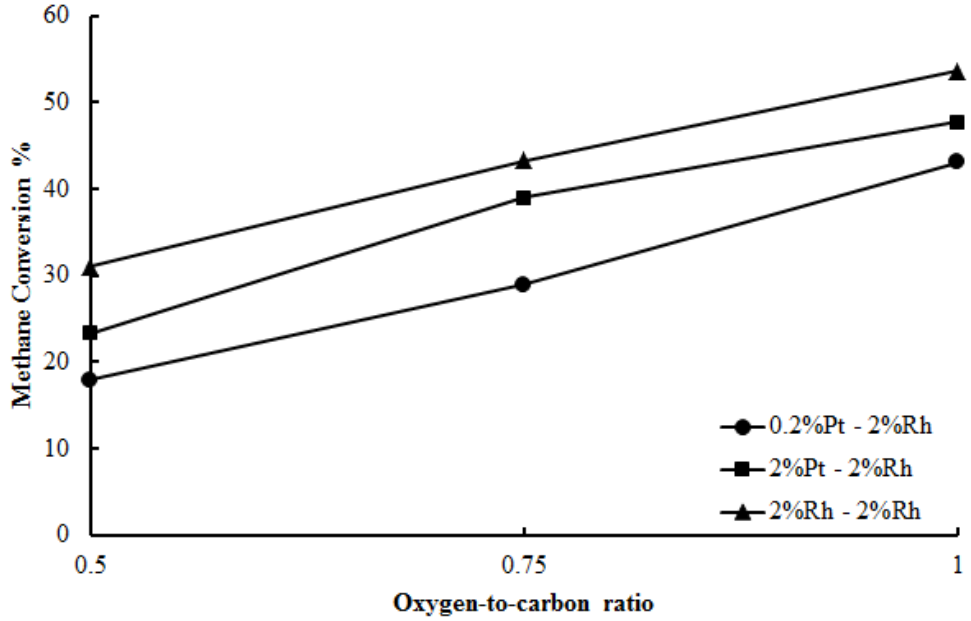

Figure 5.16. Effect of O_2/C ratio on methane conversion over 0.2wt%Pt-2wt%Rh, 2%Pt-2%Rh and 2%Rh-2%Rh (T = 700°C, H_2O/C = 1.5).

5.2.2. Hydrogen Production

In order to understand the effect of temperature, H_2O/C and O_2/C ratio on hydrogen production via OSR over 0.2wt%Pt-2wt%Rh, 2%Pt-2%Rh and 2%Rh-2%Rh catalyst combinations, the experiments are conducted for all the operating conditions given in Table 3.5. Feed compositions and flow rates are arranged as explained in Section 3.4.2 and in Table 3.6. The results are given in Tables 5.5 and 5.6 for all cases.

5.2.2.1. Effect of Temperature. When the results reported in Tables 5.5 and 5.6 are observed, it is seen that hydrogen production increases with temperature. This trend is obvious for the cases where 2%Pt-2%Rh and 2%Rh-2%Rh catalysts are used. For the case where 0.2%Pt-2%Rh catalyst is used, however, no general trend is observed. For the cases where O_2/C ratios are changed, hydrogen produced increased with temperature with the exception of the case having O_2/C ratio of 1 and H_2O/C ratio of 1.5. In this situation with the increase of oxygen partial pressure in the feed stream combustion reaction is favored, so that higher amount of water is produced. This water is

Table 5.5. Hydrogen percentages in product stream.

0.2%Pt-2%Rh						
	S/C			**O_2/C**		
T (°**C**)	1	1.25	1.5	0.5	0.75	1
600	1.67	2.76	3.68	2.04	0.77	3.68
650	0.67	2.42	3.12	3.63	3.23	3.12
700	1.51	5.25	2.96	3.79	3.22	2.96
2%Pt-2%Rh						
	S/C			**O_2/C**		
T (°**C**)	1	1.25	1.5	0.5	0.75	1
600	0.43	0.39	0.46	2.16	0.49	0.46
650	0.47	1.07	1.40	2.69	3.51	1.40
700	1.64	3.51	5.34	5.05	5.54	5.34
2%Rh-2%Rh						
	S/C			**O_2/C**		
T (°**C**)	1	1.25	1.5	0.5	0.75	1
600	0.65	0.62	0.76	2.85	1.85	0.76
650	1.81	6.54	7.83	6.06	4.43	7.83
700	9.29	8.91	7.70	8.27	9.83	7.70

Table 5.6. Amount of hydrogen produced (mol).

0.2%Pt-2%Rh						
	S/C			**O_2/C**		
T (°**C**)	1	1.25	1.5	0.5	0.75	1
600	6.83E-07	1.13E-06	1.51E-06	8.34E-07	3.13E-07	1.51E-06
650	2.73E-07	9.89E-07	1.28E-06	1.49E-06	1.32E-06	1.28E-06
700	6.19E-07	2.15E-06	1.21E-06	3.62E-06	1.32E-06	1.21E-06
2%Pt-2%Rh						
	S/C			**O_2/C**		
T (°**C**)	1	1.25	1.5	0.5	0.75	1
600	1.75E-07	1.58E-07	1.89E-07	8.83E-07	1.99E-07	1.89E-07
650	1.94E-07	4.38E-07	5.72E-07	1.10E-06	1.44E-06	5.72E-07
700	6.69E-07	1.44E-06	2.18E-06	2.07E-06	2.27E-06	2.18E-06
2%Rh-2%Rh						
	S/C			**O_2/C**		
T (°**C**)	1	1.25	1.5	0.5	0.75	1
600	2.67E-07	2.53E-07	3.11E-07	1.17E-06	7.55E-07	3.11E-07
650	7.40E-07	2.68E-06	3.20E-06	2.48E-06	1.81E-06	3.20E-06
700	3.80E-06	3.65E-06	3.15E-06	3.43E-06	4.02E-06	3.15E-06

used in SR reaction so that more hydrogen is produced. However the largest amount of hydrogen is produced for the lowest temperature 600°C. At this point, water gas shift (WGS) reaction ($CO + H_2O \rightleftharpoons CO_2 + H_2$, ΔH^0_{298} = -41.2 kJmol^{-1}) gains importance since it is shifted forward to produce more hydrogen. As temperature increases WGS is running in reverse so that hydrogen production is decreased.

5.2.2.2. Effect of H_2O/C Ratio. According to the results tabulated in Tables 5.5 and 5.6, it is seen that as H_2O/C ratio increases, the amount of hydrogen produced also increases with the exception of the experiments conducted at 700°C over 2%Rh-2%Rh catalyst. When H_2O/C ratio is increased, the increase in hydrogen production is also expected, since the amount of steam in the feed stream promotes SR equilibrium, and hence the amount of hydrogen produced. This claim is supported by experiments in which H_2O/C ratio is increased from 1 to 1.5 over 0.2%Pt-2%Rh and 2%Pt-2%Rh for all temperatures. For the case of 2%Rh-2%Rh catalyst, this phenomenon is reversed at 700°C and hydrogen production decreases as H_2O/C ratio increases. This can be explained by the behavior of WGS reaction. This temperature is very high for WGS, so that it shifts back to produce more CO by using the produced CO_2 and H_2. Since the reverse WGS becomes dominant at this temperature, its negative effects on hydrogen production cannot be compensated by SR. As more hydrogen is produced with more water addition of the system, WGS consumes more hydrogen to produce more CO which decreases the partial pressure of hydrogen in the product stream. Also it is known that the respond of SR to the amount of steam fed is non-monotonic, SR is thermodynamically favored when more steam is fed to the system, however it is not affected kinetically which explains the fluctuations seen in the H_2 production in the experiments where steam amount in the feed is changed [45].

5.2.2.3. Effect of O_2/C. According to the results tabulated in Tables 5.5 and 5.6, it is seen that there is no direct relationship observed between O_2/C ratio and hydrogen production over the three catalyst combinations investigated. When O_2 amount in the feed stream is increased, it is observed that more methane is converted via TOX. So that more H_2O is produced which should increase SR conversion and accordingly H_2

production. However the effect of O_2/C ratio on H_2 production cannot be explained in such an easy way since there is also the effect of WGS. According to the reverse and forward shift of WGS, H_2 amount produced increased or decreased as temperatures and CO and CO_2 concentrations are varied.

5.2.2.4. Effect of Catalyst Type. Experiments were carried out over three different catalyst combinations, namely 0.2%Pt-2%Rh, 2%Pt-2%Rh and 2%Rh-2%Rh. When the performances of 0.2%Pt-2%Rh and 2%Pt-2%Rh catalysts are compared, it is seen that there is not much positive effect of increasing Pt loading on hydrogen production. In several runs, the combination with 0.2%Pt delivered higher hydrogen production. For example, for the experiments conducted at 600°C and 650°C when O_2/C ratio is fixed at the value of 1, it is seen that on 0.2%Pt-2%Rh catalyst couple more hydrogen is produced than 2%Pt-2%Rh, however more hydrogen is produced on the latter one only at 700°C. This observation can be explained by the fact that, by increasing the loading of Pt, which is a very good oxidation catalyst, the amount of methane converted by TOX becomes higher. In other words, less hydrogen is produced due to reduced amounts of methane that is steam reformed. The increased TOX activity at 600 and 650°C can be verified by the higher moles of CO_2 produced (Tables 5.9 and 5.10). Therefore, it can be concluded that increasing Pt loading does not necessarily increase hydrogen production. Then the performance of 2%Pt-2%Rh and 2%Rh-2%Rh are also compared since their active metal loadings are the same. It is seen that more hydrogen is produced when 2%Rh-2%Rh is used for all cases. It is known that Rh is a very good SR catalyst when compared to Pt [45], so it is very reasonable to obtain higher H_2 production in the cases where 2%Rh-2%Rh is used. At the highest temperature tested (700°C), maximum hydrogen production of 9.83% is reached over 2%Rh-2%Rh catalysts at H_2O/C ration of 1.5 and O_2/C ratio of 0.75. The high activity of Rh is in agreement with the previous works [29].

5.2.3. Carbon Monoxide Production

In order to understand the effect of temperature, H_2O/C and O_2/C ratio on carbon monoxide production via OSR over 0.2wt%Pt-2wt%Rh, 2%Pt-2%Rh and 2%Rh-2%Rh catalyst combinations, the experiments are conducted for all the operating conditions given in Table 3.5. Feed compositions and flow rates are arranged as explained in Section 3.4.2 and in Table 3.6. The results are given in Tables 5.7 and 5.8 for all cases.

5.2.3.1. Effect of Temperature. When the results reported in Tables 5.7 and 5.8 are observed, it is seen that as temperature increases, carbon monoxide production also increases for most of the cases. In the experiments where 0.2%Pt-2%Rh catalyst, carbon monoxide production increases with incerase in temperature with the exception of one case. For the case that O_2/C ratio is fixed to 0.5 carbon monoxide production decreased when temperature is increased from 650°C to 700°C over all three catalyst combinations. This situation can be explained by the fact that there is not enough amount of oxygen in the feed stream for combustion to provide enough H_2O for the endothermic SR which leads to a decrease in the amount of CO in the product stream. When the WGS effect is taken into consideration at these temperatures, it is expected for WGS to increase CO amount at the highest temperature 700°C since it shifts backwards to produce CO by using CO_2 and H_2. But in the shortage of O_2, CO_2 production is very small which prevents WGS to convert in into CO. Other than this case where O_2/C ratio is 0.5, for all three different catalyst combinations highest amount of CO is produced at the highest temperature 700°C.

5.2.3.2. Effect of Steam-to-Carbon (H_2O/C Ratio). According to the results tabulated in Tables 5.7 and 5.8, it is seen that as H_2O/C ratio increases the amount of carbon monoxide produced tends to increase in most of the cases however this direct proportionality cannot be reported for all cases. This behavior can be explained by the balance between SR and WGS reactions. Since H_2O is reactant for both SR ($CH_4 + H_2O \rightleftharpoons CO + 3H_2$, $\Delta H^0_{298} = 206.2$ kJmol^{-1}) and WGS ($CO + H_2O \rightleftharpoons CO_2 + H_2$,

Table 5.7. Carbon monoxide percentages in product stream.

0.2%Pt-2%Rh						
	S/C			**O_2/C**		
T (°**C**)	1	1.25	1.5	0.5	0.75	1
600	1.61	2.18	2.65	1.55	0.58	2.65
650	1.65	3.23	3.11	3.25	3.06	3.11
700	3.02	4.24	5.75	3.23	4.34	5.75
2%Pt-2%Rh						
	S/C			**O_2/C**		
T (°**C**)	1	1.25	1.5	0.5	0.75	1
600	0.57	0.57	1.00	2.21	0.57	1.00
650	1.04	1.26	1.70	3.24	4.26	1.70
700	4.25	5.66	4.88	2.48	6.83	4.88
2%Rh-2%Rh						
	S/C			**O_2/C**		
T (°**C**)	1	1.25	1.5	0.5	0.75	1
600	1.15	0.77	1.17	2.57	2.47	1.17
650	2.44	3.92	3.95	2.56	3.06	3.95
700	3.26	2.71	6.74	2.36	3.46	6.74

Table 5.8. Amount of carbon monoxide produced (mol).

0.2%Pt-2%Rh						
	S/C			**O_2/C**		
T (°**C**)	1	1.25	1.5	0.5	0.75	1
600	6.58E-07	8.94E-07	1.08E-06	6.34E-07	2.38E-07	1.08E-06
650	6.77E-07	1.58E-05	1.27E-06	1.33E-06	1.25E-06	1.27E-06
700	1.24E-06	1.73E-06	2.35E-06	1.24E-06	1.78E-06	2.35E-06
2%Pt-2%Rh						
	S/C			**O_2/C**		
T (°**C**)	1	1.25	1.5	0.5	0.75	1
600	2.33E-07	2.33E-07	4.11E-07	9.04E-07	2.35E-07	4.11E-07
650	4.26E-07	5.14E-07	6.98E-07	1.32E-06	1.74E-06	6.98E-07
700	1.74E-06	2.32E-06	2.00E-06	1.01E-06	2.79E-06	2.00E-06
2%Rh-2%Rh						
	S/C			**O_2/C**		
T (°**C**)	1	1.25	1.5	0.5	0.75	1
600	4.72E-07	3.15E-07	4.80E-07	1.05E-06	1.01E-06	4.80E-07
650	9.97E-07	1.60E-06	1.62E-06	1.05E-06	1.25E-06	1.62E-06
700	1.33E-06	1.11E-06	2.76E-06	9.72E-07	1.42E-06	2.76E-06

ΔH^0_{298} = -41.2 kJmol^{-1}) reactions, understanding the effect of H_2O addition on carbon monoxide production is a complex phenomenon. Addition of H_2O increases CO production by SR however CO is consumed by WGS as H_2O amount is increased. Also as temperature changes WGS reaction shifts back or forward, i.e. CO is produced or consumed. So by taking all these variables into account, the fluctuations in CO amount produced are not unrealistic.

5.2.3.3. Effect of Oxygen-to-Carbon (O_2/C Ratio). According to the results tabulated in Tables 5.7 and 5.8, it is seen that as O_2/C ratio is changed, a general trend in the amount of carbon monoxide produced cannot be observed. The increase in O_2/C ratio has a direct effect on TOX reaction and has a slight effect on SR and WGS through CO_2 production more of which is produced by oxidation. When O_2/C ratio is increased more CO_2 is produced by TOX and in the cases of total oxygen conversion at 650 and 700°C, less methane stays reserved for SR reaction which decreases CO production via SR in the presence of excess H_2O. H_2O produced by TOX may also be used in WGS which even decreases the CO amount in the system. The balance of these three reactions becomes very sensitive when changing the oxygen amount in the feed stream, so a general trend cannot be observed because of the possible alteration of the reaction pathways by increased O_2 percentage [46].

5.2.3.4. Effect of Catalyst Type. Experiments were carried out over three different catalyst combinations, namely 0.2%Pt-2%Rh, 2%Pt-2%Rh and 2%Rh-2%Rh. When the performances of these catalysts are compared according to the CO production amounts, it is seen that there is not much noticeable difference between their CO production performances. The amount of CO produced varied within the range of 5% when all the experimental results are investigated. When 0.2%Pt-2%Rh and 2%Pt-2%Rh catalysts are compared, it is seen that very similar amount of CO is produced over both catalysts, even for some cases especially at low temperatures the performance of 0.2%Pt-2%Rh catalyst is better. As explained in Section 5.2.2.4, at 0.2%Pt-2%Rh case, due to less Pt loading less TOX occurs which leads to higher CO production per unit methane conversion. So it can be said that the amount of Pt in the catalyst does

not have a decisive effect on CO production. When 2%Pt-2%Rh and 2%Rh-2%Rh catalyst combinations are compared, it is seen that in some cases their performances are similar, however in certain cases CO production over 2%Rh-2%Rh doubled its counterpart, which is a very normal situation according to the fact that Rh is a very good SR catalyst and it favors CO production.

5.2.4. Carbon Dioxide Production

In order to understand the effect of temperature, H_2O/C and O_2/C ratio on carbon dioxide production via OSR over 0.2wt%Pt-2wt%Rh, 2%Pt-2%Rh and 2%Rh-2%Rh catalyst combinations, the experiments are conducted for all the operating conditions given in Table 3.5. Feed compositions and flow rates are arranged as explained in Section 3.4.2 and in Table 3.6. The results are given in Tables 5.9 and 5.10 for all cases.

5.2.4.1. Effect of Temperature. When the results reported in Tables 5.9 and 5.10 are observed, it is seen that as temperature increases, carbon dioxide production differs in an irregular way. CO_2 is produced by TOX and it has a part in water gas shift reaction. In WGS when the reaction shifts backward (at high temperatures) CO_2 is consumed and when it shifts forward (at low temperatures) CO_2 is produced. When the fact that there is important amount of CO_2 in the exhaust-gas stream of ICE which is used as the feed stream for this experiments is considered with all these conflicting effects, it is very normal not to expect to see a regular pattern in CO_2 production. For the experiments conducted at 650°C and 700°C complete oxygen conversion is achieved, which indicates that TOX is much faster than SR so that increasing temperature only enhances SR reaction for these cases. Also as temperature increases CO_2 is started to be consumed by WGS so in this context, after some extent it is very reasonable to observe reduction in CO_2 production because this means the fixed amount of CO_2 produced by TOX is consumed by WGS.

Table 5.9. Carbon dioxide percentages in product stream.

0.2%Pt-2%Rh						
	S/C			**O_2/C**		
T (°**C**)	1	1.25	1.5	0.5	0.75	1
600	6.76	7.49	8.23	4.28	3.97	8.23
650	8.51	10.06	12.61	4.72	7.92	12.61
700	8.10	8.57	14.37	4.80	9.22	14.37
2%Pt-2%Rh						
	S/C			**O_2/C**		
T (°**C**)	1	1.25	1.5	0.5	0.75	1
600	7.46	9.83	9.13	7.25	7.27	9.13
650	13.58	17.14	17.55	6.23	10.88	17.55
700	12.88	14.17	15.89	7.05	8.74	15.89
2%Rh-2%Rh						
	S/C			**O_2/C**		
T (°**C**)	1	1.25	1.5	0.5	0.75	1
600	11.32	16.46	18.86	7.14	12.37	18.86
650	15.39	15.64	16.97	6.83	11.81	16.97
700	14.28	16.39	14.02	7.25	11.49	14.02

Table 5.10. Amount of carbon dioxide produced (mol).

0.2%Pt-2%Rh						
	S/C			**O_2/C**		
T (°**C**)	1	1.25	1.5	0.5	0.75	1
600	2.77E-06	3.07E-06	3.37E-06	1.75E-06	1.63E-06	3.37E-06
650	3.48E-06	4.12E-06	5.16E-06	1.93E-06	3.24E-06	5.16E-06
700	3.32E-06	3.51E-06	5.88E-06	1.79E-06	3.77E-06	5.88E-06
2%Pt-2%Rh						
	S/C			**O_2/C**		
T (°**C**)	1	1.25	1.5	0.5	0.75	1
600	3.05E-06	4.02E-06	3.74E-06	2.97E-06	2.97E-06	3.74E-06
650	5.56E-06	7.01E-06	7.18E-06	2.55E-06	4.45E-06	7.18E-06
700	5.27E-06	5.80E-06	6.50E-06	2.89E-06	3.58E-06	6.50E-06
2%Rh-2%Rh						
	S/C			**O_2/C**		
T (°**C**)	1	1.25	1.5	0.5	0.75	1
600	4.63E-06	6.74E-06	7.72E-06	2.92E-06	5.06E-06	7.72E-06
650	6.30E-06	6.40E-06	6.95E-06	2.79E-06	4.83E-06	6.95E-06
700	5.84E-06	6.71E-06	5.74E-06	2.98E-06	4.70E-06	5.74E-06

5.2.4.2. Effect of H_2O/C Ratio. According to the results tabulated in Tables 5.9 and 5.10, it is seen that as H_2O/C ratio increases the amount of carbon dioxide produced tends to increase with the exception of two cases; of which over 2%Pt-2%Rh at 600°C and the other over 2%Rh-2%Rh at 700°C. H_2O addition favors CO_2 production mainly by promoting the forward WGS reaction. It is therefore expected to obtain more CO_2 with the increase of steam in the feed stream. However in some cases, because of high CO_2 concentrations and high reaction temperatures (like in the case of 2%Rh-2%Rh catalyst combination at 700°C), in the system, WGS shifts backward to consume CO_2 and produce CO. In such cases a little decrease in CO_2 production is observed. The decrease in CO_2 production at 600°C over the 2%Pt-2%Rh catalyst combination is not significant, and is most likely due to an experimental error.

5.2.4.3. Effect of O_2/C Ratio. According to the results tabulated in Tables 5.9 and 5.10, it is seen that as O_2/C ratio increases, the amount of carbon dioxide produced also increases with no exception. The increase in O_2/C ratio has great effect on TOX reaction, whereas it has an implicit effect on SR and water gas shift reaction via CO_2 synthesis. As O_2/C ratio is increased the production rate of CO_2 by TOX increases and it surpasses the rate of consumption of CO_2 by WGS even at high temperatures. Highest amount of CO_2 is obtained at 700°C over 0.2%Pt-2%Rh and at 650°C over 2%Pt-2%Rh and 2%Rh-2%Rh catalysts when O_2/C ratio is arranged to 1 and H_2O/C ratio to 1.5.

5.2.4.4. Effect of Catalyst Type. Experiments were carried out over three different catalyst combinations, namely 0.2%Pt-2%Rh, 2%Pt-2%Rh and 2%Rh-2%Rh. When the performances of 0.2%Pt-2%Rh and 2%Pt-2%Rh catalysts are compared, it can be said that the latter one is more effective when CO_2 production is considered. This results stems from the fact that as Pt loading increases TOX conversion also increases, which leads to more CO_2 production. Even the cases where reverse WGS which consumes CO_2 are considered, the reverse effect of WGS on CO_2 production is not clear which shows that TOX surpasses its effects. When 2%Pt-2%Rh and 2%Rh-2%Rh are compared, the latter delivers higher CO_2 production which shows that Rh which is very

active in SR is also a very good oxidation catalyst [26]. Highest CO_2 production of 14.4% is achieved at 700°C over 0.2%Pt-2%Rh when H_2O/C is equal to 1.5 and O_2/C is equal to 1. Over 2%Pt-2%Rh, maximum CO_2 production of 17.5% is observed at 650°C when $H_2O/C = 1.5$ and $O_2/C = 1.0$ and over 2%Rh-2%Rh maximum CO_2 production of 18.9% is observed at 600°C when $H_2O/C = 1.5$ and $O_2/C = 1.0$. Over these three catalyst combinations the feed composition giving the maximum CO_2 production is the same however in the order of 0.2%Pt-2%Rh > 2%Pt-2%Rh > 2%Rh-2%Rh, temperature to achieve maximum CO_2 decreases from 700 to 600°C which shows that at lower temperature values Rh is a better combustion catalyst than Pt.

6. CONCLUSIONS AND RECOMMENDATIONS

6.1. Conclusions

The objectives of this study were to develop a mathematical model for investigating the effects of operating conditions on propane OSR in a catalytic microchannel under EGR conditions by using CFD techniques, and to conduct experimental testing of the effects of operating conditions and catalyst types on methane OSR under EGR conditions. The conclusions drawn from this study can be summarized as follows:

- Mathematical modeling studies showed that for all types of gasoline and diesel exhaust gas compositions, temperature distribution is found to be uniform along the channel length. Comparison with packed bed and monolithic reformers showed that temperature uniformity, which is essential for improved reforming efficiencies, is much better in microchannel reactors even at low GHSV values that bring flexibility in terms of handling wide range of space velocities existing in a typical vehicular operation.
- Injecting more propane and steam into the EGR feed increased the compositions of H_2 and CO in the product stream.
- Increasing total feed flow rate, hence the GHSV led to a better temperature distribution throughout the channel, but also caused reductions in the H_2 and CO compositions in the product stream due to insufficient contact time.
- Experimental studies showed that methane conversion is directly proportional with temperature. For all feed gas composition-catalyst type combination, methane conversion increased with temperature.
- When the amount of steam is increased in the feed stream, increase in the amounts of produced hydrogen, carbon monoxide and carbon dioxide was generally observed.
- When the amount of oxygen is increased in the feed stream, no general trend was observed in the product composition due to the possible role of oxygen in changing the reaction pathways.

- When three different types of catalyst combinations (0.2%Pt-2%Rh, 2%Pt-2%Rh and 2%Rh-2%Rh) are compared, the performance of 2%Rh-2%Rh was found to be superior among the others in terms of methane conversion and hydrogen production.

6.2. Recommendations

The recommendations for enhancing this study in the context of a possible future work are listed below:

- Detailed thermodynamic analysis of the experimental system can be done in order to understand the response of product distribution against changes in the feed conditions. This thermodynamic analysis can also provide more information about the role of the particular reactions in the EGR system.
- Catalyst characterization of both fresh and spent catalysts can be done by SEM and EDX in order to determine the amounts of active metals on the catalyst surfaces as well as degree of active metal dispersions over the catalyst support.
- The parametric study can be carried out in a much wider range of temperature, O_2/C and H_2O/C ratios.
- More realistic reaction kinetics can be used to improve the mathematical model by including the presence of TOX and WGS reactions over the Rh-based catalyst.

APPENDIX A: CALIBRATION OF THE MASS FLOW CONTROLLERS

Calibration curves of the Bronkhorst F-201CV series mass flow controllers used in the experiments (Section 3) are given below.

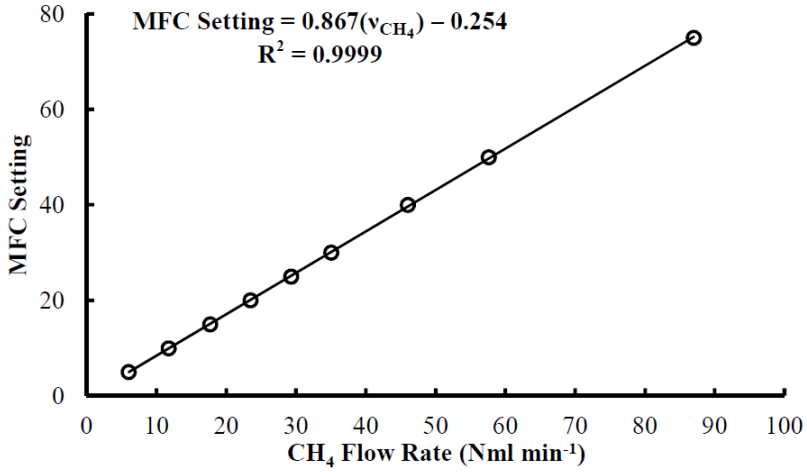

Figure A.1. Calibration curve of the methane mass flow controller.

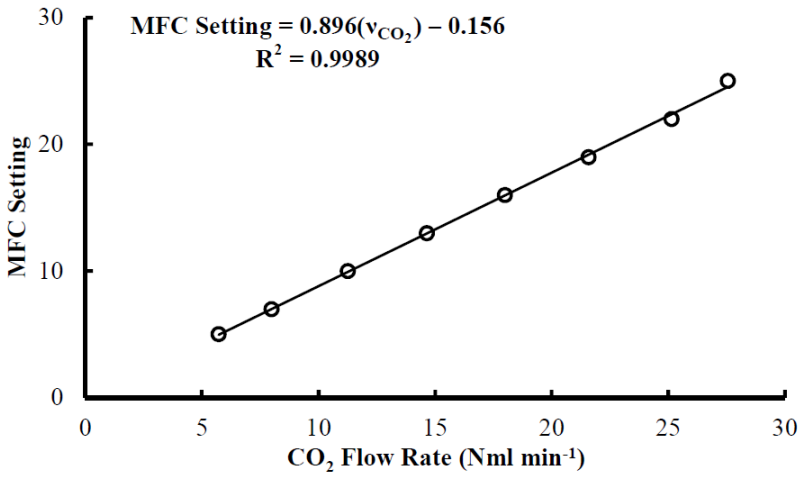

Figure A.2. Calibration curve of the carbon dioxide mass flow controller.

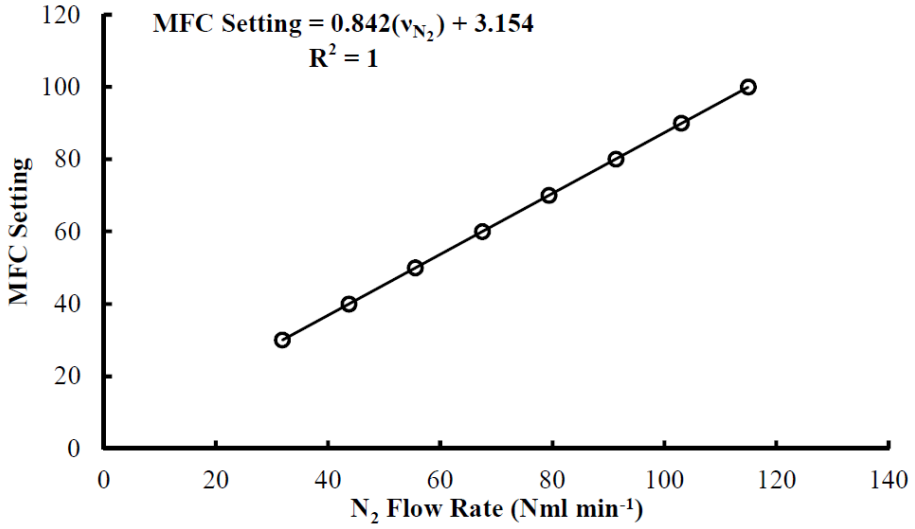

Figure A.3. Calibration curve of the nitrogen mass flow controller.

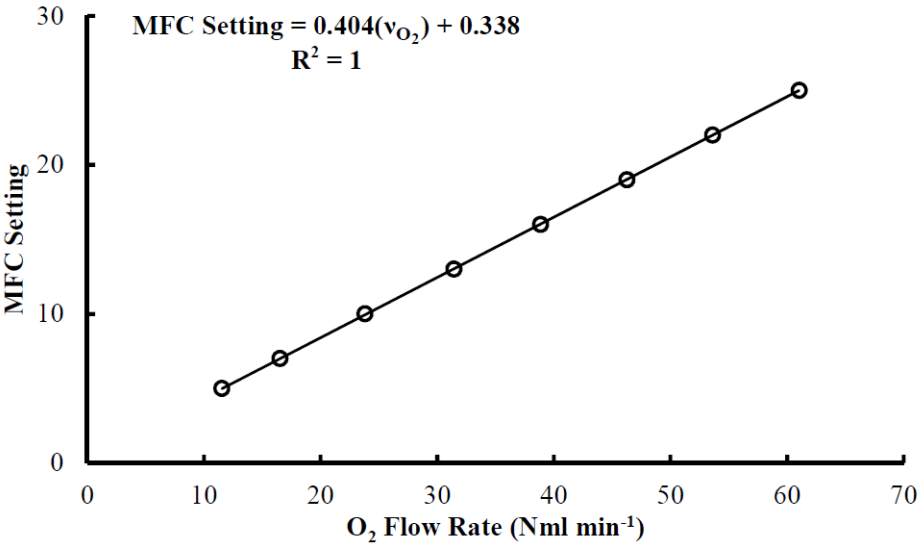

Figure A.4. Calibration curve of the oxygen mass flow controller.

APPENDIX B: CALIBRATION OF THE GAS CHROMOTOGRAPH

Calibration curves of the GC-2014 gas chromotograph used in the experiments (Section 3) are given below.

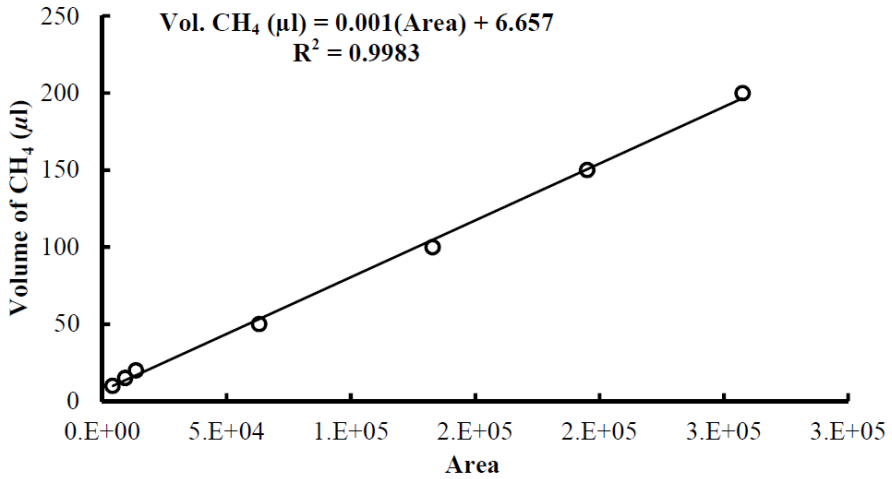

Figure B.1. GC calibration curve for methane.

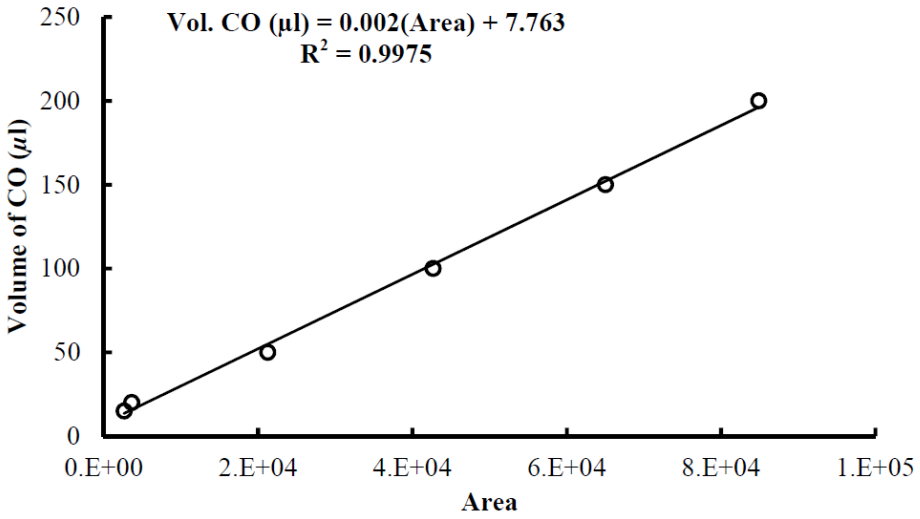

Figure B.2. GC calibration curve for carbon monoxide.

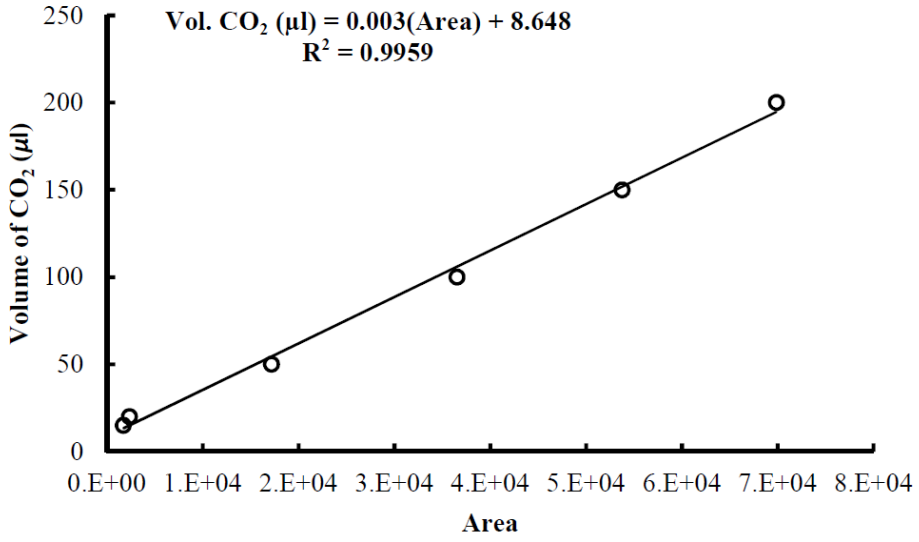

Figure B.3. GC calibration curve for carbon dioxide.

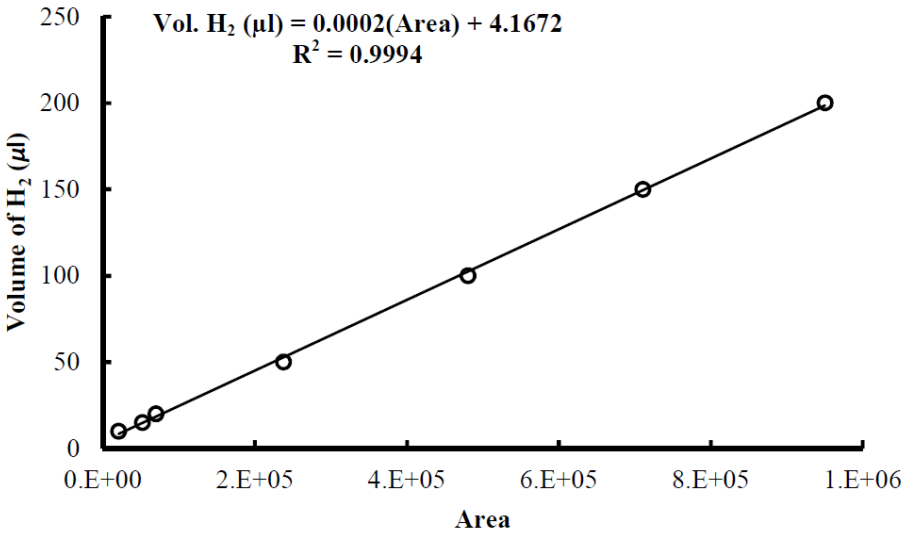

Figure B.4. GC calibration curve for hydrogen.

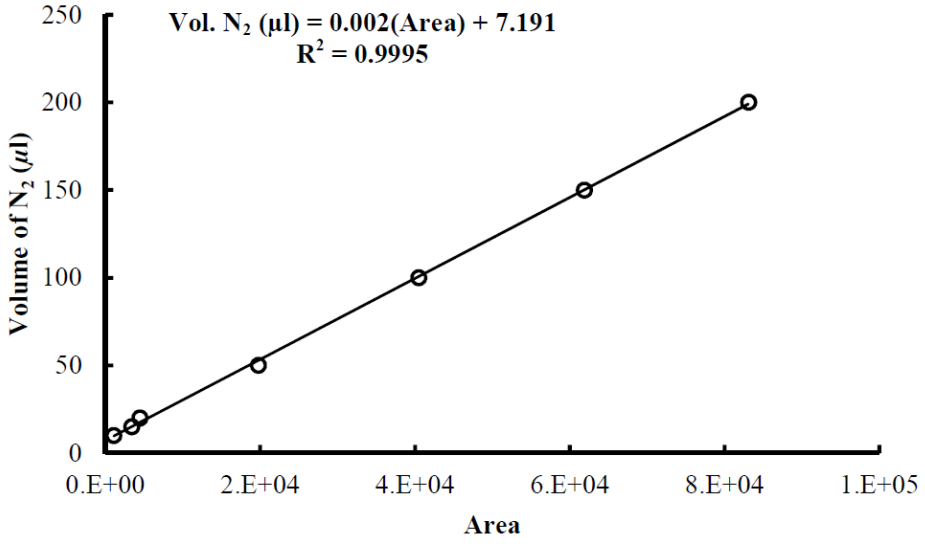

Figure B.5. GC calibration curve for nitrogen.

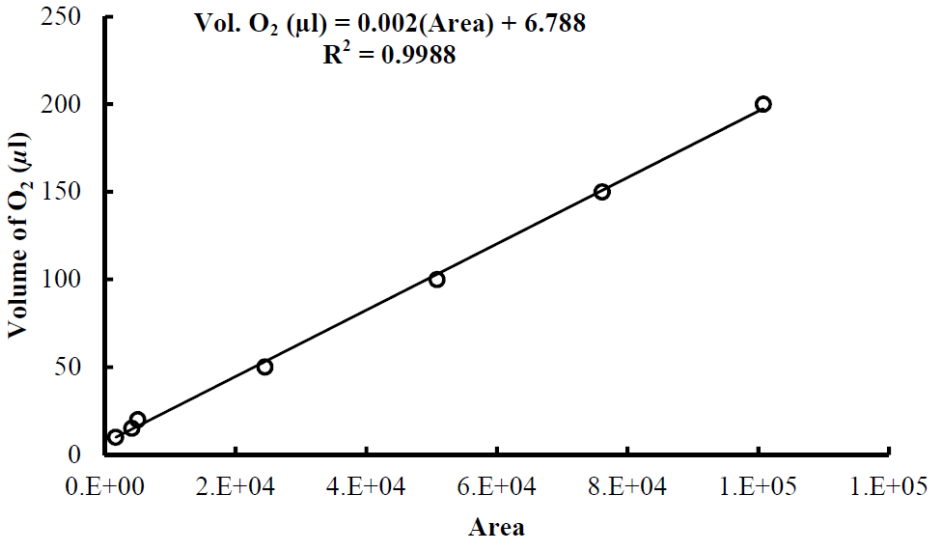

Figure B.6. GC calibration curve for oxygen.

REFERENCES

1. Golunski, S., "What is the Point of On-Board Fuel Reforming?", *Energy & Environmental Science*, Vol. 3, pp. 1918–1923, 2010.

2. Tsolakis, A. and S. Golunski, "Sensitivity of Process Efficiency to Reaction Routes in Exhaust-Gas Reforming of Diesel Fuel", *Chemical Engineering Journal*, Vol. 117, No. 2, pp. 131 – 136, 2006.

3. Tsolakis, A., A. Megaritis and S. E. Golunski, "Reaction Profiles during Exhaust-Assisted Reforming of Diesel Engine Fuels", *Energy & Fuels*, Vol. 19, No. 3, pp. 744–752, 2005.

4. Peucheret, S., M. Feaviour and S. Golunski, "Exhaust-Gas Reforming Using Precious Metal Catalysts", *Applied Catalysis B: Environmental*, Vol. 65, No. 3 – 4, pp. 201 – 206, 2006.

5. Wirth, T., *Microreactors in Organic Synthesis and Catalysis*, Wiley-VCH Verlag GmbH, Weinheim, Germany, 2008.

6. Charpentier, J., "In the Frame of Globalization and Sustainability, Process Intensification, a Path to the Future of Chemical and Process Engineering (Molecules into Money)", *Chemical Engineering Journal*, Vol. 134, pp. 84 – 92, 2007.

7. W. Ehrfeld, V. H., V. Hessel, *Microreactors, Ullmans's Encylopedia od Industrial Chemistry*, Wiley-VCH Verlag GmbH, Weinheim, Germany, 2000.

8. Kiwi-Minsker, L. and A. Renken, "Microstructured Reactors for Catalytic Reactions", *Catalysis Today*, Vol. 110, pp. 2 – 14, 2005.

9. Lerou, J., A. Tonkovich, L. Silva, S. Perry and J. McDaniel, "Microchannel Reactor Architecture Enables Greener Processes", *Chemical Engineering Science*, Vol. 65,

pp. 380 – 385, 2010.

10. Tonkovich, A., S. Perry, Y. Wang, D. Qiu, T. LaPlante and W. Rogers, "Microchannel Process Technology for Compact Methane Steam Reforming", *Chemical Engineering Science*, Vol. 59, pp. 4819 – 4824, 2004.

11. Seris, E., G. Abramowitz, A. Johnston and B. Haynes, "Scaleable, Microstructured Plant for Steam Reforming of Methane", *Chemical Engineering Journal*, Vol. 135, Supplement 1, pp. S9 – S16, 2008.

12. Hessel, V. and G. Kolb, "Microstructured Reactors for Gas Phase Reactions", *Chemical Engineering Journal*, Vol. 98, pp. 1–38, 2004.

13. Fichtner, M., J. Mayer, D. Wolf and K. Schubert, "Microstructured Rhodium Catalysts for the Partial Oxidation of Methane to Syngas under Pressure", *Industrial & Engineering Chemistry Research*, Vol. 40, pp. 3475–3483, 2001.

14. Veser, G. and J. Frauhammer, "Modelling Steady State and Ignition during Catalytic Methane Oxidation in a Monolith Reactor", *Chemical Engineering Science*, Vol. 55, pp. 2271–2286, 2000.

15. Veser, G., "Experimental and Theoretical Investigation of H_2 Oxidation in a High-Temperature Catalytic Microreactor", *Chemical Engineering Science*, Vol. 56, No. 4, pp. 1265 – 1273, 2001.

16. Hasebe, S., "Design and Operation of Micro-Chemical Plants - Bridging the Gap between Nano, Micro and Macro Technologies", *Computers & Chemical Engineering*, Vol. 29, No. 1, pp. 57 – 64, 2004.

17. Ehrfeld, W., V. Hessel and H. Löwe, *Microreactors: New Technology for Modern Chemistry*, Wiley-VCH, Mainz, 2000.

18. Schubert, K., W. Bier, J. Brandner, M. Fichtner, C. Franz and G. Linder, "Second

International Conference on Microreaction Technology (IMRET2)", p. 88, New Orleans, USA, 1998.

19. Leung, P., A. Tsolakis, J. Rodriguez-Fernandez and S. Golunski, "Raising the Fuel Heating Value and Recovering Exhaust Heat by On-Board Oxidative Reforming of Bioethanol", *Energy & Environmental Science*, Vol. 3, pp. 780–788, 2010.

20. Abu-Jrai, A., A. Tsolakis, K. Theinnoi, A. Megaritis and S. Golunski, "Diesel Exhaust-Gas Reforming for H_2 Addition to an Aftertreatment Unit", *Chemical Engineering Journal*, Vol. 141, No. 1 – 3, pp. 290 – 297, 2008.

21. Ahmed, S. and M. Krumpelt, "Hydrogen from Hydrocarbon Fuels for Fuel Cells", *International Journal of Hydrogen Energy*, Vol. 26, pp. 291–301, 2001.

22. Aartun, I., B. Silberova, H. Venvik, P. Pfeifer, O. Görke, K. Schubert and A. Holmen, "Hydrogen Production from Propane in Rh-Impregnated Metallic Microchannel Reactors and Alumina Foams", *Catalysis Today*, Vol. 105, pp. 469–478, 2005.

23. Aartun, I., H. Venvik, A. Holmen, P. Pfeifer, O. Görke and K. Schubert, "Temperature Profiles and Residence Time Effects during Catalytic Partial Oxidation and Oxidative Steam Reforming of Propane in Metallic Microchannel Reactors", *Catalysis Today*, Vol. 110, pp. 98–107, 2005.

24. Kaisare, N. S., S. R. Deshmukh and D. G. Vlachos, "Stability and Performance of Catalytic Microreactors: Simulations of Propane Catalytic Combustion on Pt", *Chemical Engineering Science*, Vol. 63, No. 4, pp. 1098 – 1116, 2008.

25. Pennemann, H., V. Hessel, G. Kolb, H. Löwe and R. Zapf, "Partial Oxidation of Propane Using Micro Structured Reactors", *Chemical Engineering Journal*, Vol. 135S, pp. S66–S73, 2008.

26. Pagani, D., D. Livio, A. Donazzi, A. Beretta, G. Groppi, M. Maestri and E. Tronconi, "A Kinetic Analysis of the Partial Oxidation of C_3H_8 over a 2% Rh/Al_2O_3

Catalyst in Annular Microreactor", *Catalysis Today*, Vol. 197, No. 1, pp. 265 – 280, 2012.

27. Tomishige, K., S. Kanazawa, K. Suzuki, M. Asadullah, M. Sato, K. Ikushima and K. Kunimori, "Effective Heat Supply from Combustion to Reforming in Methane Reforming with CO_2 and O_2: Comparison between Ni and Pt Catalysts", *Applied Catalysis A: General*, Vol. 233, pp. 35–44, 2002.

28. Li, B., K. Maruyama, M. Nurunnabi, K. Kunimori and K. Tomishige, "Temperature Profiles of Alumina-supported Noble Metal Catalysts in Autothermal Reforming of Methane", *Applied Catalysis A: General*, Vol. 275, pp. 157–172, 2004.

29. Karakaya, M. and A. K. Avci, "Parametric Study of Methane Steam Reforming to Syngas in a Catalytic Microchannel Reactor", *Applied Catalysis A: General*, Vol. 411-412, pp. 114–122, 2012.

30. Simsek, E., M. Karakaya, A. K. Avci and Z. I. Onsan, "Oxidative Steam Reforming of Methane to Synthesis Gas in Microchannel Reactors", *International Journal of Hydrogen Energy*, Vol. 38, No. 2, pp. 870 – 878, 2013.

31. Karakaya, M., *Experimental and Quantitative Analysis of Multiphase Catalytic Reactions under Microfluidic Flow Conditions and Geometries*, Ph.D. Thesis, Bogazici University, 2012.

32. Ma, L., *Hydrogen Production from Steam Reforming of Light Hydrocarbons in an Autothermic System*, Ph.D. Thesis, University of New South Wales, 1995.

33. Doesburg, E. B. M., K. P. de Jong and J. H. C. van Hooff, "Preparation of Catalyst Supports, Zeolites and Mesoporous Materials", R. A. van Santen, P. W. N. M. van Leeuwen and B. A. Averill (Editors), *Catalysis: An Integrated Approach*, pp. 433–456, Elsevier, Amsterdam, 1999.

34. Avci, A. K., D. L. Trimm, A. E. Aksoylu and Z. I. Onsan, "Hydrogen Production

by Steam Reforming of n-butane over supported Ni and Pt-Ni Catalysts", *Applied Catalysis A: General*, Vol. 258, pp. 235–240, 2004.

35. Li, Y., X. Wang, C. Xie and C. Song, "Influence of Ceria and Nickel Addition to Alumina-Supported Rh Catalyst for Propane Steam Reforming at Low Temperatures", *Applied Catalysis A: General*, Vol. 357, No. 2, pp. 213 – 222, 2009.

36. Yaws, C., *Yaws' Handbook of Thermodynamic Properties for Hydrocarbons and Chemicals*, William Andrew, Norwich, NY, USA, 2009.

37. Wilke, C., "A Viscosity Equation for Gas Mixtures", *Journal of Chemical Physics*, Vol. 18, pp. 517–519, 1950.

38. Poling, B. E., J. M. Prausnitz and J. P. O'Connell, *The Properties of Gases and Liquids*, McGraw-Hill, New York, 5th edn., 2001.

39. Bird, R. B., W. E. Stewart and E. N. Lightfoot, *Transport Phenomena*, John Wiley & Sons, New York, 2nd edn., 2002.

40. Perry, R. H. and D. W. Green, *Perry's Chemical Engineers' Handbook*, McGraw-Hill, New York, 7th edn., 1997.

41. Avci, A. K., D. L. Trimm and M. Karakaya, "Microreactor Catalytic Combustion for Chemicals Processing", *Catalysis Today*, Vol. 155, pp. 66 – 74, 2010.

42. ANSYS FLUENT 14.0 User's Guide, ANSYS Inc., Canonsburg, PA, 2011.

43. Onsan, Z. I. and A. K. Avci, "Reactor Design for Fuel Processing", D. Shekhawat, J. J. Spivey and D. A. Berry (Editors), *Fuel Cells: Technologies for Fuel Processing*, pp. 451–516, Elsevier, Amsterdam, 2011.

44. Avci, A. K., *Computational and Experimental Investigation of Catalytic hydrocarbon Fuel Processing for Autothermal Hydrogen Production*, Ph.D. Thesis, Bogazici University, 2003.

45. Avci, A., D. Trimm and Z. Onsan, "Simulation of Alternative Catalyst Bed Configurations in Autothermal Hydrogen Production", S. M. Avelino Corma, Francisco V. Melo and J. L. G. Fierro (Editors), *12th International Congress on Catalysis Proceedings of the 12th ICC*, Vol. 130, pp. 2753 – 2758, Elsevier, 2000.

46. Choudhary, V. R., A. M. Rajput and B. Prabhakar, "Nonequilibrium Oxidative Conversion of Methane to CO and H_2 with High Selectivity and Productivity over Ni/Al_2O_3 at Low Temperatures", *Journal of Catalysis*, Vol. 139, pp. 326–328, 1993.